arXiv:1706.09936v2 [hep-ex] 20 Nov 2017

Measurements of properties of the Higgs boson decaying into the four-lepton final state in pp collisions at $\sqrt{s} = 13\,\text{TeV}$

The CMS Collaboration*

Abstract

Properties of the Higgs boson are measured in the $\text{H} \rightarrow \text{ZZ} \rightarrow 4\ell$ ($\ell = \text{e}, \mu$) decay channel. A data sample of proton-proton collisions at $\sqrt{s} = 13\,\text{TeV}$, collected with the CMS detector at the LHC and corresponding to an integrated luminosity of $35.9\,\text{fb}^{-1}$ is used. The signal strength modifier μ, defined as the ratio of the observed Higgs boson rate in the $\text{H} \rightarrow \text{ZZ} \rightarrow 4\ell$ decay channel to the standard model expectation, is measured to be $\mu = 1.05^{+0.19}_{-0.17}$ at $m_\text{H} = 125.09\,\text{GeV}$, the combined ATLAS and CMS measurement of the Higgs boson mass. The signal strength modifiers for the individual Higgs boson production modes are also measured. The cross section in the fiducial phase space defined by the requirements on lepton kinematics and event topology is measured to be $2.92\,^{+0.48}_{-0.44}\,(\text{stat})\,^{+0.28}_{-0.24}\,(\text{syst})\,\text{fb}$, which is compatible with the standard model prediction of $2.76 \pm 0.14\,\text{fb}$. Differential cross sections are reported as a function of the transverse momentum of the Higgs boson, the number of associated jets, and the transverse momentum of the leading associated jet. The Higgs boson mass is measured to be $m_\text{H} = 125.26 \pm 0.21\,\text{GeV}$ and the width is constrained using the on-shell invariant mass distribution to be $\Gamma_\text{H} < 1.10\,\text{GeV}$, at 95% confidence level.

*See Appendix A for the list of collaboration members

1   Introduction

In 2012, the ATLAS and CMS Collaborations reported the observation of a new particle with a mass of approximately 125 GeV and properties consistent with that of the standard model (SM) Higgs boson [1–3]. Further studies by the two experiments [4–6], using the entire LHC Run 1 data set at center-of-mass energies of 7 and 8 TeV indicate agreement within their uncertainties between the measured properties of the new boson and those predicted for the SM Higgs boson [7–12]. The ATLAS and CMS Collaborations have also published a combined measurement of the Higgs boson mass of $m_H = 125.09 \pm 0.21\,\text{(stat)} \pm 0.11\,\text{(syst)}\,\text{GeV}$ [13].

The $H \to ZZ \to 4\ell$ decay channel ($\ell = e, \mu$) has a large signal-to-background ratio, and the precise reconstruction of the final-state decay products allows the complete determination of the kinematics of the Higgs boson. This makes it one of the most important channels to measure the properties of the Higgs boson. Measurements performed by the ATLAS and CMS Collaborations using this decay channel with the LHC Run 1 data include the determination of the mass and spin-parity of the boson [14–18], its width [19–21], the fiducial cross sections [22, 23], and the tensor structure of its interaction with a pair of neutral gauge bosons [16, 18, 20].

In this paper measurements of properties of the Higgs boson decaying into the four-lepton final state in proton-proton (pp) collisions at $\sqrt{s} = 13\,\text{TeV}$ are presented. Events are classified into categories optimized with respect to those used in Ref. [14] to provide increased sensitivity to subleading production modes of the Higgs boson such as vector boson fusion (VBF) and associated production with a vector boson (WH, ZH) or top quark pair (ttH). The signal strength modifier, defined as the ratio of the measured Higgs boson rate in the $H \to ZZ \to 4\ell$ decay channel to the SM expectation, is measured. The signal strength modifiers for the individual Higgs boson production modes are constrained. In addition, cross section measurements and dedicated measurements of the mass and width of the Higgs boson are performed.

This paper is structured as follows: the apparatus and the data samples are described in Section 2 and Section 3. Section 4 summarizes the event reconstruction and selection. Kinematic discriminants and event categorization are discussed in Section 5 and Section 6. The background estimation and the signal modelling are reported in Section 7 and Section 8. We then discuss the systematic uncertainties in Section 9. Finally, Section 10 presents event yields, kinematic distributions, and measured properties.

2   The CMS detector

A detailed description of the CMS detector, together with a definition of the coordinate system used and the relevant kinematic variables, can be found in Ref. [24].

The central feature of the CMS apparatus is a superconducting solenoid of 6 m internal diameter, providing a magnetic field of 3.8 T. Within the solenoid volume are a silicon pixel and strip tracker, a lead tungstate crystal electromagnetic calorimeter (ECAL), and a brass and scintillator hadron calorimeter (HCAL), each composed of a barrel and two endcap sections. Forward calorimeters extend the pseudorapidity (η) coverage provided by the barrel and endcap detectors. Muons are detected in gas-ionization chambers embedded in the steel flux-return yoke outside the solenoid.

The silicon tracker measures charged particles within the pseudorapidity range $|\eta| < 2.5$. It consists of 1440 silicon pixel and 15 148 silicon strip detector modules. For non-isolated particles with transverse momentum p_T between 1 and 10 GeV and $|\eta| < 1.4$, the track resolutions are typically 1.5% in p_T and 25–90 (45–150) μm in the transverse (longitudinal) impact parame-

ter [25].

The electromagnetic calorimeter consists of 75 848 lead tungstate crystals, which provide coverage in pseudorapidity $|\eta| < 1.479$ in the barrel region (EB) and $1.479 < |\eta| < 3.0$ in the two endcap regions (EE). A preshower detector consisting of two planes of silicon sensors interleaved with a total of $3X_0$ of lead is located in front of the EE. The electron momentum is estimated by combining the energy measurement in the ECAL with the momentum measurement in the tracker. The momentum resolution for electrons with $p_T \approx 45\,\text{GeV}$ from $Z \to ee$ decays ranges from 1.7% for electrons in the barrel region that do not shower in the tracker volume to 4.5% for electrons in the endcaps that do shower in the tracker volume [26].

Muons are measured in the pseudorapidity range $|\eta| < 2.4$, with detection planes made using three technologies: drift tubes, cathode strip chambers, and resistive plate chambers. Matching muons to tracks measured in the silicon tracker results in a relative transverse momentum resolution for muons with $20 < p_T < 100\,\text{GeV}$ of 1.3–2.0% in the barrel ($|\eta| < 0.9$) and better than 6% in the endcaps ($|\eta| > 0.9$). The p_T resolution in the barrel is better than 10% for muons with p_T up to 1 TeV [27].

The first level (L1) of the CMS trigger system [28], composed of custom hardware processors, uses information from the calorimeters and muon detectors to select the most interesting events in a fixed time interval of less than $4\,\mu$s. The high-level trigger (HLT) processor farm further decreases the event rate from around 100 kHz to less than 1 kHz, before data storage.

3 Data and simulated samples

This analysis makes use of pp collision data recorded by the CMS detector in 2016, corresponding to an integrated luminosity of $35.9\,\text{fb}^{-1}$. Collision events are selected by high-level trigger algorithms that require the presence of leptons passing loose identification and isolation requirements. The main triggers of this analysis select either a pair of electrons or muons, or an electron and a muon. The minimal transverse momentum with respect to the beam axis of the leading electron (muon) is 23 (17) GeV, while that of the subleading lepton is 12 (8) GeV. To maximize the signal acceptance, triggers requiring three leptons with lower p_T thresholds and no isolation requirement are also used, as are isolated single-electron and single-muon triggers with the thresholds of 27 GeV and 22 GeV, respectively. The overall trigger efficiency for simulated signal events that pass the full selection chain of this analysis (described in Section 4) is larger than 99%. The trigger efficiency is measured in data with a method based on the "tag-and-probe" technique [29] using a sample of 4ℓ events collected by the single-lepton triggers. Leptons passing the single-lepton triggers are used as tags and the other three leptons are used as probes. The efficiency in data is found to be in agreement with the expectation from simulation.

The Monte Carlo (MC) simulation samples for the signals and the relevant background processes are used to estimate backgrounds, optimize the event selection, and evaluate the acceptance and systematic uncertainties. The SM Higgs boson signals are generated at next-to-leading order (NLO) in perturbative quantum chromodynamics (pQCD) with the POWHEG 2.0 [30–32] generator for the five main production modes: gluon fusion (gg $\to$ H), vector boson fusion (qq $\to$ qqH), and associated production (WH, ZH, and t$\bar{\text{t}}$H). For WH and ZH the MINLO HVJ [33] extension of POWHEG 2.0 is used. The cross sections for the various signal processes are taken from Ref. [34], and in particular the cross section for the dominant gluon fusion production mode is taken from Ref. [35]. The default set of parton distribution functions (PDFs) used in all simulations is NNPDF30_nlo_as_0118 [36]. The decay of the Higgs boson to four

leptons is modeled with JHUGEN 7.0.2 [37, 38]. In the case of ZH and tt̄H, the Higgs boson is also allowed to decay as H → ZZ → 2ℓ2X where X stands for either a quark or a neutrino, thus accounting for four-lepton events where two leptons originate from the decay of the associated Z boson or top quarks. In all of the simulated samples, vector bosons are allowed to decay to τ-leptons such that this contribution is included in all estimations.

To generate a more accurate signal model, the p_T spectrum of the Higgs boson was tuned in the POWHEG simulation of the dominant gluon fusion production mode to better match predictions from full phase space calculations implemented in the HRES 2.3 generator [39, 40].

The SM ZZ background contribution from quark-antiquark annihilation is generated at NLO pQCD with POWHEG 2.0, while the gg → ZZ process is generated at leading order (LO) with MCFM [41].

All signal and background generators are interfaced with PYTHIA 8.212 [42] tune CUETP8M1 [43] to simulate multiple parton interactions, the underlying event, and the fragmentation and hadronization effects. The generated events are processed through a detailed simulation of the CMS detector based on GEANT4 [44, 45] and are reconstructed with the same algorithms that are used for data. The simulated events include overlapping pp interactions (pileup) and have been reweighted so that the distribution of the number of interactions per LHC bunch crossing in simulation matches that observed in data.

4 Event reconstruction and selection

Event reconstruction is based on the particle-flow (PF) algorithm [46], which exploits information from all the CMS subdetectors to identify and reconstruct individual particles in the event. The PF candidates are classified as charged hadrons, neutral hadrons, photons, electrons, or muons, and they are then used to build higher-level observables such as jets and lepton isolation quantities.

Electrons with $p_T^e > 7\,\text{GeV}$ are reconstructed within the geometrical acceptance defined by a pseudorapidity $|\eta^e| < 2.5$. Electrons are identified using a multivariate discriminant that includes observables sensitive to the presence of bremsstrahlung along the electron trajectory, the geometrical and momentum-energy matching between the electron trajectory and the associated energy cluster in the ECAL, the shape of the electromagnetic shower in the ECAL, and variables that discriminate against electrons originating from photon conversions such as the number of expected but missing pixel hits and the conversion vertex fit probability.

Muons within the geometrical acceptance $|\eta^\mu| < 2.4$ and $p_T^\mu > 5\,\text{GeV}$ are reconstructed by combining information from the silicon tracker and the muon system [27]. The matching between the inner and outer tracks proceeds either outside-in, starting from a track in the muon system, or inside-out, starting from a track in the silicon tracker. In the latter case, tracks that match track segments in only one or two planes of the muon system are also considered in the analysis to collect very low-p_T muons that may not have sufficient energy to penetrate the entire muon system. The muons are selected among the reconstructed muon track candidates by applying minimal requirements on the track in both the muon system and inner tracker system, and taking into account compatibility with small energy deposits in the calorimeters.

To suppress muons originating from in-flight decays of hadrons and electrons from photon conversions, we require each lepton track to have the ratio of the impact parameter in three dimensions, computed with respect to the chosen primary vertex position, and its uncertainty to be less than 4. The primary vertex is defined as the reconstructed vertex with the largest

value of summed physics-object p_T^2, where the physics objects are the objects returned by a jet finding algorithm [47, 48] applied to all charged tracks associated with the vertex, plus the corresponding associated missing transverse energy, E_T^{miss}, defined as the magnitude of the vector sum of the transverse momenta of all reconstructed PF candidates (charged or neutral) in the event.

To discriminate between prompt leptons from Z boson decay and those arising from electroweak decays of hadrons within jets, an isolation requirement for leptons of $\mathcal{I}^\ell < 0.35$ is imposed, where the relative isolation is defined as

$$\mathcal{I}^\ell \equiv \left(\sum p_T^{charged} + \max\left[0, \sum p_T^{neutral} + \sum p_T^\gamma - p_T^{PU}(\ell)\right] \right) / p_T^\ell. \tag{1}$$

The isolation sums involved are all restricted to a volume bounded by a cone of angular radius $\Delta R = 0.3$ around the lepton direction at the primary vertex, where the angular distance between two particles i and j is $\Delta R(i,j) = \sqrt{(\eta^i - \eta^j)^2 + (\phi^i - \phi^j)^2}$. The $\sum p_T^{charged}$ is the scalar sum of the transverse momenta of charged hadrons originating from the chosen primary vertex of the event. The $\sum p_T^{neutral}$ and $\sum p_T^\gamma$ are the scalar sums of the transverse momenta for neutral hadrons and photons, respectively. Since the isolation variable is particularly sensitive to energy deposits from pileup interactions, a $p_T^{PU}(\ell)$ contribution is subtracted, using two different techniques. For muons, we define $p_T^{PU}(\mu) \equiv 0.5 \sum_i p_T^{PU,i}$, where i runs over the momenta of the charged hadron PF candidates not originating from the primary vertex, and the factor of 0.5 corrects for the different fraction of charged and neutral particles in the cone. For electrons, the FASTJET technique [48–50] is used, in which $p_T^{PU}(e) \equiv \rho A_{eff}$, where the effective area A_{eff} is the geometric area of the isolation cone scaled by a factor that accounts for the residual dependence of the average pileup deposition on the η of the electron, and ρ is the median of the p_T density distribution of neutral particles within the area of any jet in the event.

An algorithm is used to recover the final-state radiation (FSR) from leptons. Photons reconstructed by the PF algorithm within $|\eta_\gamma| < 2.4$ are considered as FSR candidates if they pass $p_T^\gamma > 2\,\text{GeV}$ and $\mathcal{I}^\gamma < 1.8$, where the photon relative isolation $\mathcal{I}^\gamma$ is defined as for the leptons in Eq. 1. Associating every such photon to the closest selected lepton in the event, we discard photons that do not satisfy $\Delta R(\gamma, \ell)/(p_T^\gamma)^2 < 0.012\,\text{GeV}^{-2}$ and $\Delta R(\gamma, \ell) < 0.5$. We finally retain the lowest-$\Delta R(\gamma, \ell)/(p_T^\gamma)^2$ photon candidate of every lepton, if any. Photons thus identified are excluded from any isolation computation.

The momentum scale and resolution for electrons and muons are calibrated in bins of p_T^ℓ and η^ℓ using the decay products of known dilepton resonances. The electron momentum scale is corrected with a $Z \to e^+e^-$ sample by matching the peak of the reconstructed dielectron mass spectrum in data to the one in simulation. A pseudorandom Gaussian smearing is applied to electron energies in simulation to make the $Z \to e^+e^-$ mass resolution match the one in data [51]. Muon momenta are calibrated using a Kalman filter approach [52], using J/ψ meson and Z boson decays.

A "tag-and-probe" technique based on inclusive samples of Z boson events in data and simulation is used to measure the efficiency of the reconstruction and selection for prompt electrons and muons in several bins of p_T^ℓ and η^ℓ. The difference in the efficiencies measured in simulation and data, which on average is 1% (4%) per muon (electron), is used to rescale the selection efficiency in the simulated samples.

Jets are reconstructed from the PF candidates, clustered by the anti-k_T algorithm [47, 48] with a distance parameter of 0.4, and with the constraint that the charged particles are compatible with the primary vertex. The jet momentum is determined as the vector sum of all particle

momenta in the jet, and is found in the simulation to reproduce the true momentum at the 5 to 10% level over the whole p_T spectrum and detector acceptance. Jet energy scale corrections are derived from the simulation and confirmed with measurements examining the energy balance in dijet, multijet, $\gamma +$ jet, and leptonic $Z/\gamma +$ jet events [53, 54]. Jet energies in simulation are smeared to match the resolution in data. To be considered in the analysis, jets must satisfy $p_T^{\text{jet}} > 30\,\text{GeV}$ and $|\eta^{\text{jet}}| < 4.7$, and be separated from all selected lepton candidates and any selected FSR photon by $\Delta R(\ell/\gamma, \text{jet}) > 0.4$.

For event categorization, jets are tagged as b-jets using the Combined Secondary Vertex algorithm [55, 56] which combines information about the impact parameter significance, the secondary vertex and the jet kinematics. The variables are combined using a multilayer perceptron approach to compute the b tagging discriminator. Data-to-simulation scale factors for the b tagging efficiency are applied as a function of jet p_T, η, and flavor. The E_T^{miss} is also used for the event categorization.

The event selection is designed to extract signal candidates from events containing at least four well-identified and isolated leptons, each originating from the primary vertex and possibly accompanied by an FSR photon candidate. In what follows, unless otherwise stated, FSR photons are included in invariant mass computations.

First, Z boson candidates are formed with pairs of leptons (e^+e^-, $\mu^+\mu^-$) of the same flavor and opposite sign (OS) and required to pass $12 < m_{\ell^+\ell^-} < 120\,\text{GeV}$. They are then combined into ZZ candidates, wherein we denote as Z_1 the Z candidate with an invariant mass closest to the nominal Z boson mass (m_Z) [57], and as Z_2 the other one. The flavors of the leptons involved define three mutually exclusive subchannels: 4e, 4μ, and 2e2μ.

To be considered for the analysis, ZZ candidates have to pass a set of kinematic requirements that improve the sensitivity to Higgs boson decays. The Z_1 invariant mass must be larger than 40 GeV. All leptons must be separated in angular space by at least $\Delta R(\ell_i, \ell_j) > 0.02$. At least two leptons are required to have $p_T > 10\,\text{GeV}$ and at least one is required to have $p_T > 20\,\text{GeV}$. For Z_1Z_2 candidates composed of four same flavor leptons, an alternative pairing Z_aZ_b can be formed out of the same four leptons. We discard the Z_1Z_2 candidate if $m(Z_a)$ is closer to m_Z than $m(Z_1)$ and $m(Z_b) < 12\,\text{GeV}$. This protects against events that contain an on-shell Z and a low-mass dilepton resonance. In events with only four leptons this requirement leads to the event being discarded, while in events with more than four leptons other ZZ candidates are considered. To further suppress events with leptons originating from hadron decays in jet fragmentation or from the decay of low-mass hadronic resonances, all four OS lepton pairs that can be built with the four leptons (irrespective of flavor) are required to satisfy $m_{\ell^+\ell^-} > 4\,\text{GeV}$, where selected FSR photons are disregarded in the invariant mass computation. Finally, the four-lepton invariant mass $m_{4\ell}$ must be larger than 70 GeV.

In events where more than one ZZ candidate passes the above selection, the candidate with the highest value of $\mathcal{D}_{\text{bkg}}^{\text{kin}}$ (defined in Section 5) is retained, except when two candidates consist of the same four leptons in which case the candidate with the Z_1 mass closest to m_Z is retained. The additional leptons that do not form the ZZ candidate but pass identification, vertex compatibility, and isolation requirements are used in the event categorization, see Section 6.

5 Kinematic discriminants and event-by-event mass uncertainty

The full kinematic information from each event using either the Higgs boson decay products or associated particles in its production is extracted using matrix element calculations and is

used to form several kinematic discriminants. These computations rely on the MELA package [37, 38, 58] and use JHUGEN matrix elements for the signal and MCFM matrix elements for the background. The decay kinematics of the scalar H boson and the production kinematics of gluon fusion in association with one jet (H+1 jet) or two jets (H+2 jets), VBF, ZH, and WH associated production are explored in this analysis. The kinematics of the full event are described by decay observables $\vec{\Omega}^{H \to 4\ell}$ or observables describing associated production $\vec{\Omega}^{H+JJ}$. The definition of these observables can be found in Refs. [37, 38, 58].

The discriminant sensitive to the $gg/q\bar{q} \to 4\ell$ kinematics is calculated as [2, 16]

$$\mathcal{D}_{bkg}^{kin} = \left[1 + \frac{\mathcal{P}_{bkg}^{q\bar{q}}(\vec{\Omega}^{H \to 4\ell}|m_{4\ell})}{\mathcal{P}_{sig}^{gg}(\vec{\Omega}^{H \to 4\ell}|m_{4\ell})} \right]^{-1}, \tag{2}$$

where $\mathcal{P}_{sig}^{gg}$ is the probability density for an event to be consistent with the signal and $\mathcal{P}_{bkg}^{q\bar{q}}$ is the corresponding probability density for the dominant $q\bar{q} \to ZZ \to 4\ell$ background process, all calculated either with the JHUGEN or MCFM matrix elements within the MELA framework.

Four discriminants are used to enhance the purity of event categories as described in Section 6. $\mathcal{D}_{2\,jet}$ is the discriminant sensitive to the VBF signal topology with two associated jets, $\mathcal{D}_{1\,jet}$ is the discriminant sensitive to the VBF signal topology with one associated jet, and $\mathcal{D}_{WH}$ or $\mathcal{D}_{ZH}$ are the discriminants sensitive to the ZH or WH signal topologies with two associated jets from the decay of the $Z \to q\bar{q}$ or the $W \to q\bar{q}'$:

$$\mathcal{D}_{2\,jet} = \left[1 + \frac{\mathcal{P}_{HJJ}(\vec{\Omega}^{H+JJ}|m_{4\ell})}{\mathcal{P}_{VBF}(\vec{\Omega}^{H+JJ}|m_{4\ell})} \right]^{-1} \qquad \mathcal{D}_{1\,jet} = \left[1 + \frac{\mathcal{P}_{HJ}(\vec{\Omega}^{H+J}|m_{4\ell})}{\int d\eta_J \mathcal{P}_{VBF}(\vec{\Omega}^{H+JJ}|m_{4\ell})} \right]^{-1}$$

$$\mathcal{D}_{WH} = \left[1 + \frac{\mathcal{P}_{HJJ}(\vec{\Omega}^{H+JJ}|m_{4\ell})}{\mathcal{P}_{WH}(\vec{\Omega}^{H+JJ}|m_{4\ell})} \right]^{-1} \qquad \mathcal{D}_{ZH} = \left[1 + \frac{\mathcal{P}_{HJJ}(\vec{\Omega}^{H+JJ}|m_{4\ell})}{\mathcal{P}_{ZH}(\vec{\Omega}^{H+JJ}|m_{4\ell})} \right]^{-1} \tag{3}$$

where $\mathcal{P}_{VBF}$, $\mathcal{P}_{HJJ}$, $\mathcal{P}_{HJ}$, and $\mathcal{P}_{VH}$ are probability densities obtained from the JHUGEN matrix elements for the VBF, H + 2 jets, H + 1 jet, and VH (V = W, Z) processes, respectively. The expression $\int d\eta_J \mathcal{P}_{VBF}$ is the integral of the two-jet VBF matrix element probability density discussed above over the η_J values of the unobserved jet with the constraint that the total transverse momentum of the H + 2 jets system is zero. By construction, all discriminants defined in Eqs. 2 and 3 have values bounded between 0 and 1.

The uncertainty in the momentum measurement can be predicted for each lepton. For muons, the full covariance matrix is obtained from the muon track fit, and the directional uncertainties are negligibly small. For the electrons, the momentum uncertainty is estimated from the combination of the ECAL and tracker measurements, neglecting the uncertainty in the track direction. The uncertainty in the kinematics at the per-lepton level is then propagated to the four-lepton candidate to predict the mass uncertainty ($\mathcal{D}_{mass}$) on an event-by-event basis. For FSR photons, a parametrization obtained from simulation is used for the uncertainty in the photon p_T. The per-lepton momentum uncertainties are corrected in data and simulation using Z boson events. Events are divided into different categories based on the predicted dilepton mass resolution. A Breit–Wigner parameterization convolved with a double-sided Crystal Ball function [59] is then fit to the dilepton mass distribution in each category to extract the resolution and compare it to the predicted resolution. Corrections to the lepton momentum uncertainty are derived through an iterative procedure in different bins of lepton p_T and η. After the corrections are derived, a closure test of the agreement between the predicted and fitted 4ℓ mass resolution is

performed in data and in simulation, in bins of the predicted 4ℓ mass resolution, confirming that the calibration brings it close to the fitted value. A systematic uncertainty of 20% in the 4ℓ mass resolution is assigned to cover the residual differences between the predicted and fitted resolutions.

6   Event categorization

To improve the sensitivity to the various Higgs boson production mechanisms, the selected events are classified into mutually exclusive categories. The category definitions exploit the jet multiplicity, the number of b-tagged jets, the number of additional leptons (defined as leptons that pass identification, vertex compatibility, and isolation requirements, but do not form the ZZ candidate), and requirements on the kinematic discriminants described in Section 5.

Seven categories are defined, using the criteria applied in the following order (i.e. an event is considered for the subsequent category only if it does not satisfy the requirements of the previous category):

- The VBF-2jet-tagged category requires exactly four leptons. In addition, there must be either two or three jets of which at most one is b tagged, or four or more jets none of which are b-tagged. Finally, $\mathcal{D}_{2\,\text{jet}} > 0.5$ is required.

- The VH-hadronic-tagged category requires exactly four leptons. In addition, there must be two or three jets, or four or more jets none of which are b-tagged. $\mathcal{D}_{\text{VH}} \equiv \max(\mathcal{D}_{\text{ZH}}, \mathcal{D}_{\text{WH}}) > 0.5$ is required.

- The VH-leptonic-tagged category requires no more than three jets and no b-tagged jets in the event, and exactly one additional lepton or one additional pair of OS, same-flavor leptons. This category also includes events with no jets and at least one additional lepton.

- The t$\bar{\text{t}}$H-tagged category requires at least four jets of which at least one is b tagged, or at least one additional lepton.

- The VH-$E_{\text{T}}^{\text{miss}}$-tagged category requires exactly four leptons, no more than one jet and $E_{\text{T}}^{\text{miss}}$ greater than 100 GeV.

- The VBF-1jet-tagged category requires exactly four leptons, exactly one jet and $\mathcal{D}_{1\,\text{jet}} > 0.5$.

- The Untagged category consists of the remaining selected events.

The definitions of the categories were chosen to achieve high signal purity whilst maintaining high efficiency for each of the main Higgs boson production mechanisms. The order of the categories is chosen to maximize the signal purity target in each category. Figure 1 shows the relative signal purity of the seven event categories for the various Higgs boson production processes. The VBF-1jet-tagged and VH-hadronic-tagged categories are expected to have substantial contamination from gluon fusion, while the purity of the VBF process in the VBF-2jet-tagged category is expected to be about 49%.

7   Background estimation

7.1   Irreducible backgrounds

The irreducible backgrounds to the Higgs boson signal in the 4ℓ channel, which come from the production of ZZ via q$\bar{\text{q}}$ annihilation or gluon fusion, are estimated using simulation. The
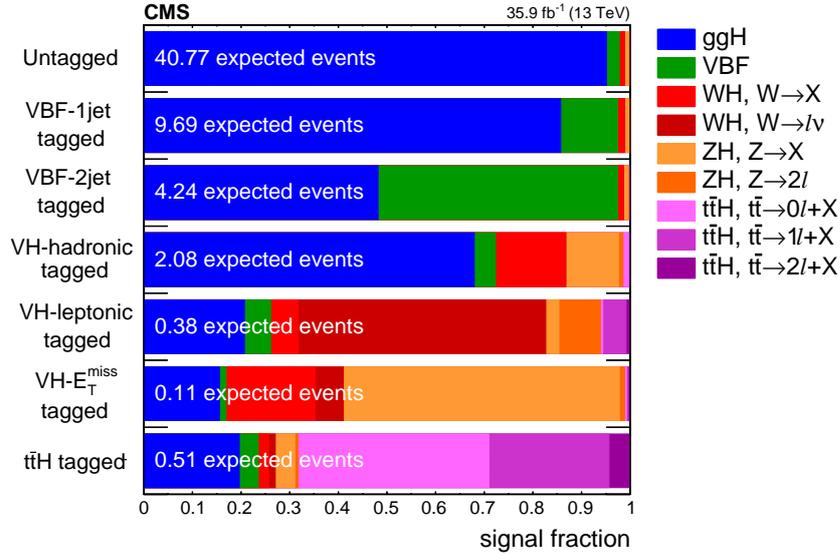
Figure 1: Relative signal purity in the seven event categories in terms of the five main production mechanisms of the Higgs boson in the $118 < m_{4\ell} < 130$ GeV mass window are shown. The WH, ZH, and t$\bar{\text{t}}$H processes are split according to the decay of the associated particles, where X denotes anything other than an electron or a muon. Numbers indicate the total expected signal event yields in each category.

fully differential cross section for the $q\bar{q} \rightarrow ZZ$ process has been computed at next-to-next-to-leading order (NNLO) [60], and the NNLO/NLO K-factor as a function of m_{ZZ} has been applied to the POWHEG sample. This K-factor varies from 1.0 to 1.2 and is 1.1 at $m_{ZZ} = 125$ GeV. Additional NLO electroweak corrections, which depend on the initial state quark flavor and kinematics, are also applied in the region $m_{ZZ} > 2m_Z$ where the corrections have been computed [61]. The uncertainty due to missing electroweak corrections in the region $m_{ZZ} < 2m_Z$ is expected to be small compared to the uncertainties in the pQCD calculation.

The production of ZZ via gluon fusion contributes at NNLO in pQCD. It has been shown [62] that the soft-collinear approximation is able to describe the background cross section and the interference term at NNLO. Further calculations also show that at NLO the K-factor for the signal and background [63] and at NNLO the K-factor for the signal and interference terms [64] are very similar. Therefore, the same K-factor used for the signal is also used for the background [65]. The NNLO K-factor for the signal is obtained as a function of m_{ZZ} using the HNNLO v2 program [40, 66, 67] by calculating the NNLO and LO gg $\rightarrow$ H $\rightarrow 2\ell 2\ell'$ cross sections at the small H boson decay width of 4.1 MeV and taking their ratios. The NNLO/LO K-factor for gg $\rightarrow$ ZZ varies from 2.0 to 2.6 and is 2.27 at $m_{ZZ} = 125$ GeV; a systematic uncertainty of 10% in its determination when applied to the background process is used in the analysis.

7.2   Reducible backgrounds

Additional backgrounds to the Higgs boson signal in the 4ℓ channel arise from processes in which heavy flavor jets produce secondary leptons, and also from processes in which decays of heavy flavor hadrons, in-flight decays of light mesons within jets, or (for electrons) the decay of charged hadrons overlapping with π^0 decays, are misidentified as prompt leptons. We denote these reducible backgrounds as "Z+X" since the dominant process producing them is Z + jets, while subdominant processes in order of importance are t$\bar{\text{t}}$ + jets, Zγ + jets, WZ + jets, and

WW + jets. In the case of $Z\gamma$ + jets, the photon may convert to an e^+e^- pair with one of the decay products not being reconstructed, giving rise to a signature with three prompt leptons. The contribution from the reducible background is estimated using two independent methods having dedicated control regions in data. The control regions are defined by a dilepton pair satisfying all the requirements of a Z_1 candidate and two additional leptons, OS or same-sign (SS), satisfying certain relaxed identification requirements when compared to those used in the analysis. These four leptons are then required to pass the ZZ candidate selection. The event yield in the signal region is obtained by weighting the control region events by the lepton misidentification probability (or misidentification rate) f, defined as the fraction of nonsignal leptons that are identified by the analysis selection criteria.

The lepton misidentification rates f_e and f_μ are determined from data, separately for the SS and OS methods, using a control region defined by a Z_1 candidate and exactly one additional lepton passing the relaxed selection. The Z_1 candidate consists of a pair of leptons, each of which passes the selection requirements used in the analysis. For the OS method, the mass of the Z_1 candidate is required to satisfy $|m(Z_1) - m_Z| < 7\,\text{GeV}$ to reduce the contribution of (asymmetric) photon conversions, which is estimated separately. In the SS method, the contribution from photon conversions is estimated by determining an average misidentification rate. Furthermore the E_T^{miss} is required to be less than $25\,\text{GeV}$ to suppress contamination from WZ and $t\bar{t}$ processes. The fraction of these events in which the additional lepton passes the selection requirements used in the analysis gives the lepton misidentification rate f. The lepton misidentification rates is measured as a function of p_T^ℓ and $|\eta^\ell|$ and is assumed to be independent of the presence of any additional leptons.

7.2.1   Method using OS leptons

The control region for the OS method consists of events with a Z_1 candidate and two additional OS leptons of the same-flavor. The expected yield in the signal region is obtained from two categories of events.

The first category is composed of events with two leptons that pass (P) the tight lepton identification requirements and two leptons that pass the loose identification but fail (F) the tight identification, and is denoted as the 2P2F region. Backgrounds, which intrinsically have only two prompt leptons, such as Z + jets and $t\bar{t}$, are estimated with this control region. To obtain the expected yield in the signal region, each event i in the 2P2F region is weighted by a factor $[f_3^i/(1-f_3^i)][f_4^i/(1-f_4^i)]$, where f_3^i and f_4^i are the misidentification rates for the third and fourth lepton, respectively.

The second category consists of events where exactly one of the two additional leptons passes the analysis selection, and is referred to as the 3P1F region. Backgrounds with three prompt leptons, such as WZ + jets and $Z\gamma$ + jets with the photon converting to e^+e^-, are estimated using this region. To obtain the expected yield in the signal region, each event j in the 3P1F region is weighted by a factor $f_4^j/(1-f_4^j)$, where f_4^j is the misidentification rate for the lepton that does not pass the analysis selection. The contribution from ZZ events to the 3P1F region ($N_{3\text{P1F}}^{ZZ}$), which arises from events where a prompt lepton fails the identification requirements, is estimated from simulation and scaled with a factor w_{ZZ} appropriate to the integrated luminosity of the analyzed data set.

The contamination of 2P2F-type processes in the 3P1F region is estimated as $\sum_i\{[f_3^i/(1-f_3^i)] + [f_4^i/(1-f_4^i)]\}$ and contributes an amount equal to $\sum_i\{2[f_3^i/(1-f_3^i)][f_4^i/(1-f_4^i)]\}$ to the expected yield in the signal region. This amount is subtracted from the total background estimate to avoid double counting.

The total reducible background estimate in the signal region coming from the two categories 2P2F and 3P1F without double counting, $N_{\mathrm{SR}}^{\mathrm{reducible}}$, can be written as:

$$N_{\mathrm{SR}}^{\mathrm{reducible}} = \sum_{j}^{N_{\mathrm{3P1F}}} \frac{f_4^j}{1 - f_4^j} - w_{\mathrm{ZZ}} \sum_{j}^{N_{\mathrm{3P1F}}^{\mathrm{ZZ}}} \frac{f_4^j}{1 - f_4^j} - \sum_{i}^{N_{\mathrm{2P2F}}} \frac{f_3^i}{1 - f_3^i} \frac{f_4^i}{1 - f_4^i},\tag{4}$$

where N_{3P1F} and N_{2P2F} are the number of events in the 3P1F and 2P2F regions, respectively.

7.2.2   Method using SS leptons

The control region for the SS method, referred to as the $2\mathrm{P2L}_{\mathrm{SS}}$ region, consists of events with a Z_1 candidate and two additional SS leptons of same-flavor. These two additional leptons are required to pass the loose selection requirements for leptons.

The contribution of photon conversions to the electron misidentification probability f is estimated. Its linear dependence on the fraction of loose electrons in the sample with tracks having one missing hit in the pixel detector, r_{miss}, is used to derive a corrected misidentification rate $\tilde{f}$. The dependence is determined by measuring f in samples with different values of r_{miss} formed by varying the requirements on $|m_{\ell_1\ell_2} - m_Z|$ and $|m_{\ell_1\ell_2\mathrm{e}_{\mathrm{loose}}} - m_Z|$. Here ℓ_1 and ℓ_2 are the leptons which form the Z_1 candidate and $\mathrm{e}_{\mathrm{loose}}$ is the additional electron passing the loose selection.

The expected number of reducible background events in the signal region can then be written as:

$$N_{\mathrm{SR}}^{\mathrm{reducible}} = r_{\mathrm{OS/SS}} \sum_{i}^{N_{\mathrm{2P2L}_{\mathrm{SS}}}} \tilde{f}_3^i \tilde{f}_4^i,\tag{5}$$

where the ratio $r_{\mathrm{OS/SS}}$ between the number of events in the $2\mathrm{P2L}_{\mathrm{OS}}$ and $2\mathrm{P2L}_{\mathrm{SS}}$ control regions is obtained from simulation. The $2\mathrm{P2L}_{\mathrm{OS}}$ region is defined analogously to the $2\mathrm{P2L}_{\mathrm{SS}}$ region but with an OS requirement for the additional pair of loose leptons.

7.2.3   Prediction and uncertainties

The predicted yield in the signal region of the reducible background from the two methods are in agreement within their statistical uncertainties, and since they are mutually independent, the results of the two methods are combined. The final estimate is obtained by weighting the individual mean values of both methods according to their corresponding variances. The shape of the $m_{4\ell}$ distribution for the reducible background is obtained by combining the prediction from the OS and SS methods and fitting the distributions with empirical functional forms built from Landau [68] and exponential distributions.

The dominant systematic uncertainty in the reducible background estimation arises from the limited number of events in the control regions as well as in the region where the misidentification rate is applied. Additional sources of systematic uncertainty, estimated using simulated samples, come from the fact that the composition of the regions used to compute the misidentification rates typically differs from that of control regions where they are applied. The subdominant systematic uncertainty in the $m_{4\ell}$ shape is determined by taking the envelope of differences among the shapes from the OS and SS methods in the three different final states. The combined systematic uncertainty is estimated to be about 40%.

8   Signal modeling

The signal shape of a narrow resonance around $m_{\mathrm{H}} \sim 125\,\mathrm{GeV}$ is parametrized using a double-sided Crystal Ball function. The signal shape is parametrized as a function of m_{H} by performing

a simultaneous fit of several mass points for gg $\rightarrow$ H production around 125 GeV. Each parameter of the double-sided Crystal Ball function is given a linear dependence on m_H for a total of 12 free parameters. Of these parameters, 10 are left free in the simultaneous fits. The parameters that control the prominence of the tails in the two Crystal Ball functions are forced to have a unique value at all m_H values, to remove large correlations and because they are constant within the uncertainty. This parameterization, derived separately for each 4ℓ final state, is found to provide a good description of the resonant part of the signal for all production modes and event categories. An additional non-resonant contribution from WH, ZH, and $t\bar{t}$H production arises when one of the leptons from the Higgs boson decay is lost or is not selected. This contribution is modeled by a Landau distribution which is added to the total probability density function for those production modes.

For the measurement of the width the signal shape for a broad resonance around $m_H \sim 125$ GeV is parameterized in the following way. First, the gluon fusion or electroweak (VBF and VH) signal production is treated jointly with the corresponding background and their interference as:

$$\mathcal{P}^i(m_{4\ell}; m_H, \Gamma_H) = \mu_i \, \mathcal{P}^i_{\text{sig}}(m_{4\ell}; m_H, \Gamma_H) + \mathcal{P}^i_{\text{bkg}}(m_{4\ell}) + \sqrt{\mu_i} \mathcal{P}_{\text{int}}(m_{4\ell}; m_H, \Gamma_H), \qquad (6)$$

where μ_i is the signal strength in the production type i, gluon fusion or electroweak, and the small $t\bar{t}$H contribution is treated jointly with gluon fusion. The general parameterization of the probability density function in Eq. (6) is based on the framework of MCFM + JHUGEN + HNNLO within MELA. The ideal parameterization is based on the matrix element calculation with the H boson propagator removed from the cross section scans as a function of $m_{4\ell}$. The propagator is included analytically with m_H and Γ_H as unconstrained parameters of the model. Detector effects are included via the multiplicative efficiency function $\mathcal{E}(m_{4\ell})$ and convolution for the mass resolution $\mathcal{R}(m_{4\ell}|m_{4\ell}^{\text{truth}})$, both extracted from the full simulation in the same way as for the narrow resonance discussed above. The resulting distribution is

$$\mathcal{P}^{\text{reco}}(m_{4\ell}) = \left(\mathcal{E}(m_{4\ell}^{\text{truth}}) \, \mathcal{P}(m_{4\ell}^{\text{truth}}; m_H, \Gamma_H) \right) \otimes \mathcal{R}(m_{4\ell}|m_{4\ell}^{\text{truth}}). \qquad (7)$$

9 Systematic uncertainties

The experimental uncertainties common to all measurements include the uncertainty in the integrated luminosity measurement (2.5%) [69] and the uncertainty in the lepton identification and reconstruction efficiency (ranging from 2.5 to 9% on the overall event yield for the 4μ and 4e channels), which affect both signal and background. Experimental uncertainties in the reducible background estimation, described in Section 7.2, vary between 36% (4μ) and 43% (4e).

The uncertainty in the lepton energy scale, which is the dominant source of systematic uncertainty in the Higgs boson mass measurement, is determined by considering the $Z \rightarrow \ell\ell$ mass distributions in data and simulation. Events are separated into categories based on the p_T and η of one of the two leptons, selected randomly, and integrating over the other. A Breit–Wigner parameterization convolved with a double-sided Crystal Ball function is then fit to the dilepton mass distributions. The offsets in the measured peak position with respect to the nominal Z boson mass in data and simulation are extracted, and the results are shown in Fig. 2. In the case of electrons, since the same data set is used to derive and validate the momentum scale corrections, the size of the corrections is taken into account for the final value of the uncertainty. The 4ℓ mass scale uncertainty is determined to be 0.04%, 0.3%, and 0.1% for the 4μ, 4e, and 2e2μ channels, respectively. The uncertainty in the 4ℓ mass resolution coming from the uncertainty in the per-lepton energy resolution is 20%, as described in Section 5.
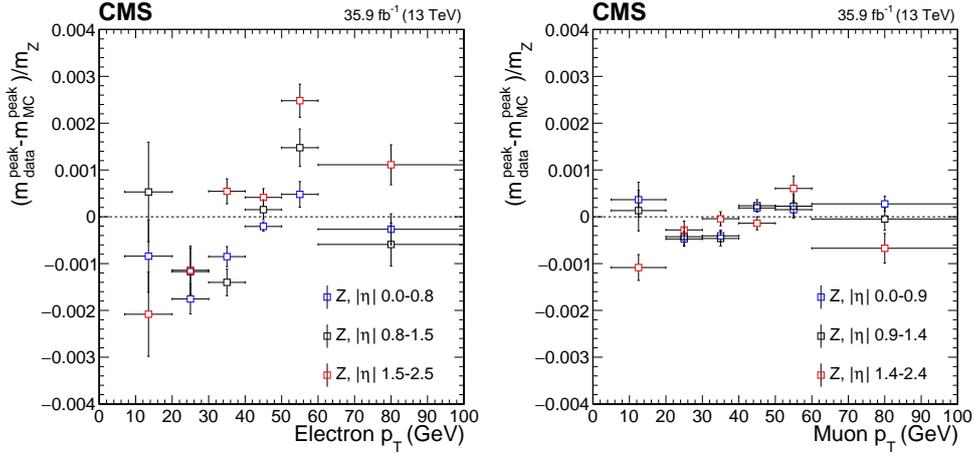
Figure 2: Difference between the $Z \to \ell\ell$ mass peak positions in data ($m_{\text{data}}^{\text{peak}}$) and simulation ($m_{\text{MC}}^{\text{peak}}$) normalized by the nominal Z boson mass (m_Z), as a function of the p_T and $|\eta|$ of one of the leptons regardless of the second for electrons (left) and muons (right).

Theoretical uncertainties that affect both the signal and background estimation include uncertainties from the renormalization and the factorization scales and the choice of the PDF set. The uncertainty from the renormalization and factorization scale is determined by varying these scales between 0.5 and 2 times their nominal value while keeping their ratio between 0.5 and 2. The uncertainty from the PDF set is determined following the PDF4LHC recommendations [70]. An additional uncertainty of 10% in the K factor used for the gg $\to$ ZZ prediction is applied as described in Section 7.1. A systematic uncertainty of 2% [34] in the H $\to$ 4ℓ branching fraction only affects the signal yield. The theoretical uncertainties in the background yield are included for all measurements, while the theoretical uncertainties in the overall signal yield are not included in the measurement uncertainties when cross sections, rather than signal strength modifiers, are extracted.

In the case of the measurements which use event categorization, experimental and theoretical uncertainties that account for possible migration of signal and background events between categories are included. The main sources of uncertainty in the event categorization include the renormalization and factorization scales, PDF set, and the modeling of the fragmentation, hadronization, and the underlying event. These uncertainties amount to 4–20% for the signal and 3–20% for the background, depending on the category, and are largest for the prediction of the gg $\to$ H yield in the VBF-2jet-tagged category. Additional uncertainties come from the imprecise knowledge of the jet energy scale (from 2% for the gg $\to$ H yield in the untagged category to 15% for the gg $\to$ H yield in the VBF-2jet-tagged category) and b tagging efficiency and mistag rate (up to 6% in the t$\bar{\text{t}}$H-tagged category).

10   Results

The reconstructed four-lepton invariant mass distribution is shown in Fig. 3 for the sum of the 4e, 4μ, and 2e2μ channels, and compared with the expectations from signal and background processes. The error bars on the data points correspond to the so-called Garwood confidence intervals at 68% confidence level (CL) [71]. The observed distribution agrees with the expectation within the statistical uncertainties over the whole spectrum. In Fig. 4, the reconstructed four-lepton invariant mass distributions are split by event category, for the low-mass range.
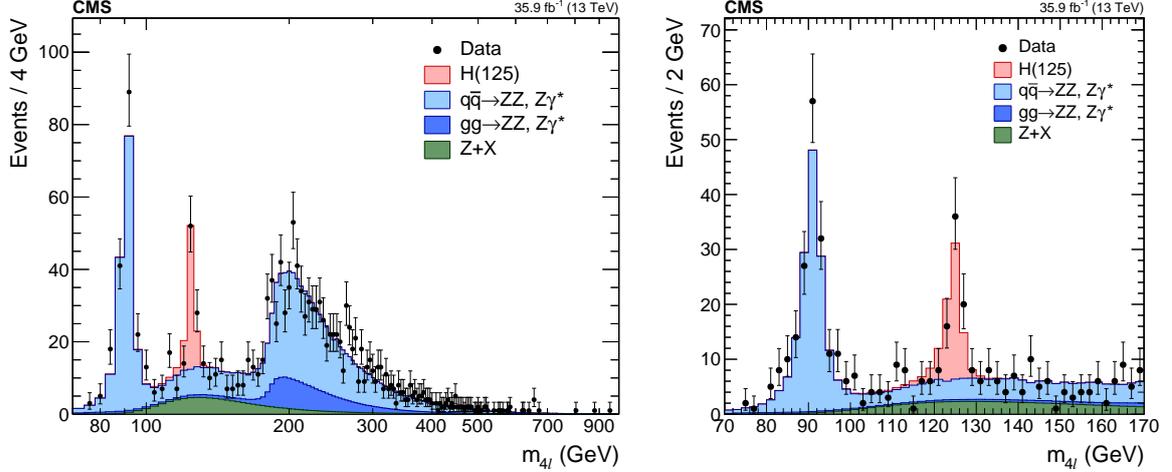
Figure 3: Distribution of the reconstructed four-lepton invariant mass $m_{4\ell}$ in the full mass range (left) and the low-mass range (right). Points with error bars represent the data and stacked histograms represent expected signal and background distributions. The SM Higgs boson signal with $m_H = 125$ GeV, denoted as H(125), and the ZZ backgrounds are normalized to the SM expectation, whilst the Z+X background is normalized to the estimation from data. The order in perturbation theory used for the normalization of the irreducible backgrounds is described in Section 7.1. No events are observed with $m_{4\ell} > 1$ TeV.

The number of candidates observed in data and the expected yields for the backgrounds and the Higgs boson signal after the full event selection are reported in Table 1 for $m_{4\ell} > 70$ GeV. Table 2 shows the expected and observed yields for each of the seven event categories and their total.

Table 1: The numbers of expected background and signal events and the number of observed candidate events after the full selection, for each final state, for $m_{4\ell} > 70$ GeV. The signal and ZZ backgrounds are estimated from simulation, while the Z+X event yield is estimated from data. Uncertainties include statistical and systematic sources.

Channel	4e	4μ	2e2μ	4ℓ
$q\bar{q} \to ZZ$	193^{+19}_{-20}	360^{+25}_{-27}	471^{+33}_{-36}	1024^{+69}_{-76}
$gg \to ZZ$	$41.2^{+6.3}_{-6.1}$	$69.0^{+9.5}_{-9.0}$	102^{+14}_{-13}	212^{+29}_{-27}
Z+X	$21.1^{+8.5}_{-10.4}$	34^{+14}_{-13}	60^{+27}_{-25}	115^{+32}_{-30}
Sum of backgrounds	255^{+24}_{-25}	463^{+32}_{-34}	633^{+44}_{-46}	1351^{+86}_{-91}
Signal	$12.0^{+1.3}_{-1.4}$	23.6 ± 2.1	30.0 ± 2.6	65.7 ± 5.6
Total expected	267^{+25}_{-26}	487^{+33}_{-35}	663^{+46}_{-47}	1417^{+89}_{-94}
Observed	293	505	681	1479

The reconstructed dilepton invariant masses for the selected Z_1 and Z_2 candidates are shown in Fig. 5 for $118 < m_{4\ell} < 130$ GeV, along with their correlation. Figure 6 shows the correlation between the kinematic discriminant $\mathcal{D}^{\text{kin}}_{\text{bkg}}$ with the four-lepton invariant mass, the two variables used in the likelihood fit to extract the results (see Section 10.1). The gray scale represents the expected combined relative density of the ZZ background and the Higgs boson signal. The points show the data and the measured four-lepton mass uncertainties $\mathcal{D}_{\text{mass}}$ as horizontal bars. Different marker colors and styles are used to denote the final state and the categorization of the events, respectively. This distribution shows that the two observed events around 125 GeV in the VH-E_T^{miss}-tagged and ttH-tagged categories (empty star and square markers) have low
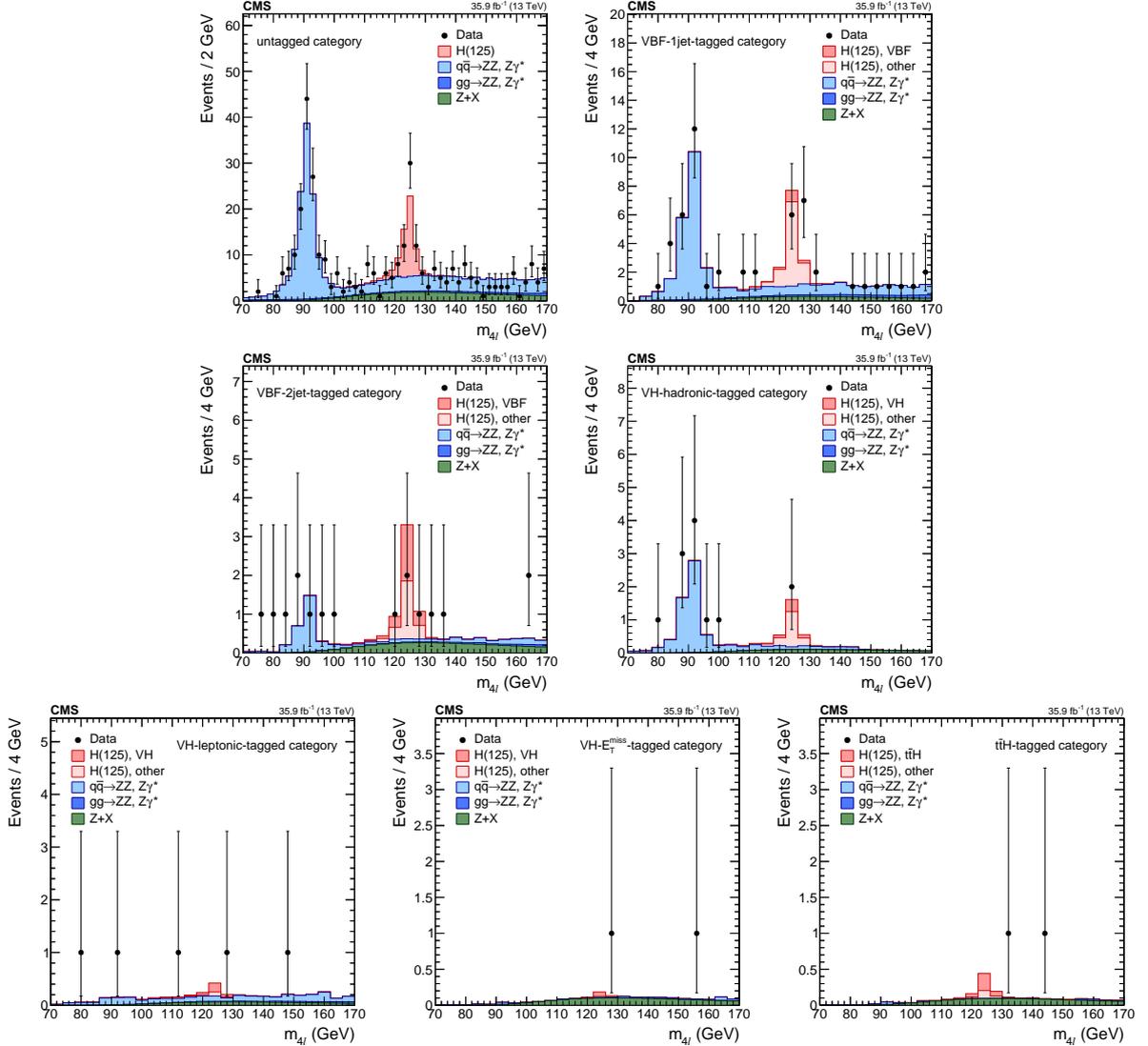
Figure 4: Distribution of the reconstructed four-lepton invariant mass in the seven event categories for the low-mass range. (Top left) untagged category. (Top right) VBF-1jet-tagged category. (Center left) VBF-2jet-tagged category. (Center right) VH-hadronic-tagged category. (Bottom left) VH-leptonic-tagged category. (Bottom middle) VH-E_T^{miss}-tagged category. (Bottom right) t$\bar{t}$H-tagged category. Points with error bars represent the data and stacked histograms represent expected signal and background distributions. The SM Higgs boson signal with $m_H = 125$ GeV, denoted as H(125), and the ZZ backgrounds are normalized to the SM expectation, whilst the Z+X background is normalized to the estimation from data. For the categories other than the untagged category, the SM Higgs boson signal is separated into two components: the production mode that is targeted by the specific category, and other production modes, where the gluon fusion dominates. The order in perturbation theory used for the normalization of the irreducible backgrounds is described in Section 7.1.

Table 2: The numbers of expected background and signal events and the number of observed candidate events after the full selection, for each event category, for the mass range $118 < m_{4\ell} < 130\,\text{GeV}$. The yields are given for the different production modes. The signal and ZZ backgrounds yields are estimated from simulation, while the Z+X yield is estimated from data.

	Event category							
	Untagged	VBF-1j	VBF-2j	VH-hadr.	VH-lept.	VH-$E_{\text{T}}^{\text{miss}}$	$t\bar{t}$H	Inclusive
$q\bar{q} \to ZZ$	19.18	2.00	0.25	0.30	0.27	0.01	0.01	22.01
$gg \to ZZ$	1.67	0.31	0.05	0.02	0.04	0.01	<0.0	2.09
Z+X	10.79	0.88	0.78	0.31	0.17	0.30	0.27	13.52
Sum of backgrounds	31.64	3.18	1.08	0.63	0.49	0.32	0.28	37.62
uncertainties	$+4.30$ -3.42	$+0.37$ -0.32	$+0.29$ -0.21	$+0.13$ -0.09	$+0.07$ -0.07	$+0.14$ -0.11	$+0.09$ -0.07	$+5.19$ -4.18
$gg \to H$	38.78	8.31	2.04	1.41	0.08	0.02	0.10	50.74
VBF	1.08	1.14	2.09	0.09	0.02	<0.01	0.02	4.44
WH	0.43	0.14	0.05	0.30	0.21	0.03	0.02	1.18
ZH	0.41	0.11	0.04	0.24	0.04	0.07	0.02	0.93
$t\bar{t}$H	0.08	<0.01	0.02	0.03	0.02	<0.01	0.35	0.50
Signal	40.77	9.69	4.24	2.08	0.38	0.11	0.51	57.79
uncertainties	$+3.69$ -3.62	$+1.13$ -1.17	$+0.55$ -0.55	$+0.23$ -0.23	$+0.03$ -0.03	$+0.01$ -0.02	$+0.06$ -0.06	$+4.89$ -4.80
Total expected	72.41	12.88	5.32	2.71	0.86	0.43	0.79	95.41
uncertainties	$+7.35$ -6.27	$+1.25$ -1.21	$+0.78$ -0.65	$+0.34$ -0.28	$+0.10$ -0.09	$+0.15$ -0.12	$+0.14$ -0.12	$+9.86$ -8.32
Observed	73	13	4	2	1	1	0	94

values of $\mathcal{D}_{\text{bkg}}^{\text{kin}}$, implying that these events are more compatible with the background than the signal hypothesis. The distribution of the discriminants used for event categorization and the corresponding working point values are shown in Fig. 7.
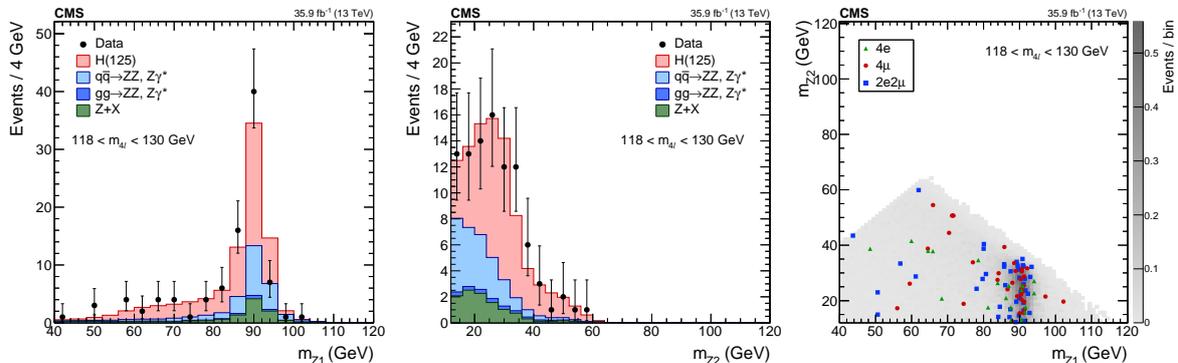

Figure 5: Distribution of the Z_1 (left) and Z_2 (middle) reconstructed invariant masses and two-dimensional distribution of these two variables (right) in the mass region $118 < m_{4\ell} < 130\,\text{GeV}$. The stacked histograms and the gray scale represent the expected signal and background distributions, and points represent the data. The SM Higgs boson signal with $m_{\text{H}} = 125\,\text{GeV}$, denoted as H(125), and the ZZ backgrounds are normalized to the SM expectation, whilst the Z+X background is normalized to the estimation from data. The order in perturbation theory used for the normalization of the irreducible backgrounds is described in Section 7.1.
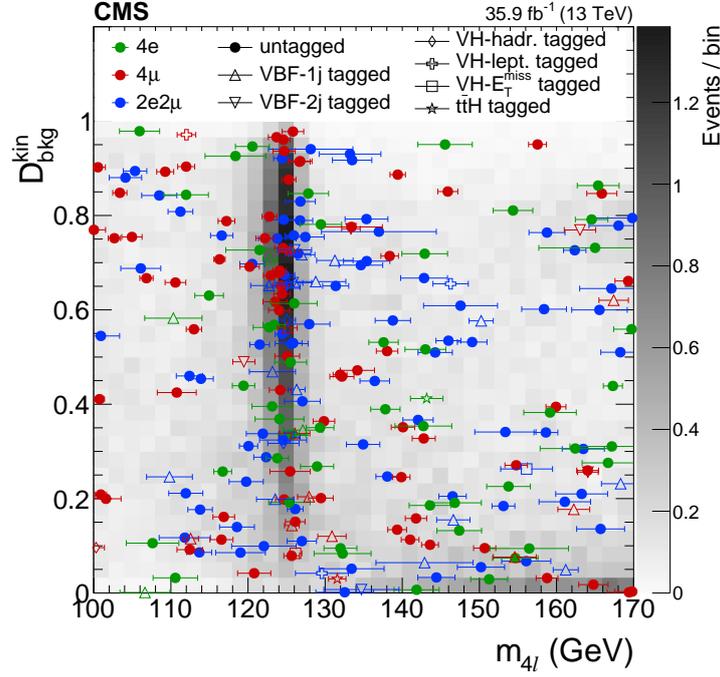
Figure 6: Distribution of $\mathcal{D}_{\mathrm{bkg}}^{\mathrm{kin}}$ versus $m_{4\ell}$ in the mass region $100 < m_{4\ell} < 170\,\mathrm{GeV}$. The gray scale represents the expected total number of ZZ background and SM Higgs boson signal events for $m_{\mathrm{H}} = 125\,\mathrm{GeV}$. The points show the data and the horizontal bars represent $\mathcal{D}_{\mathrm{mass}}$. Different marker colors and styles are used to denote final state and the categorization of the events, respectively.
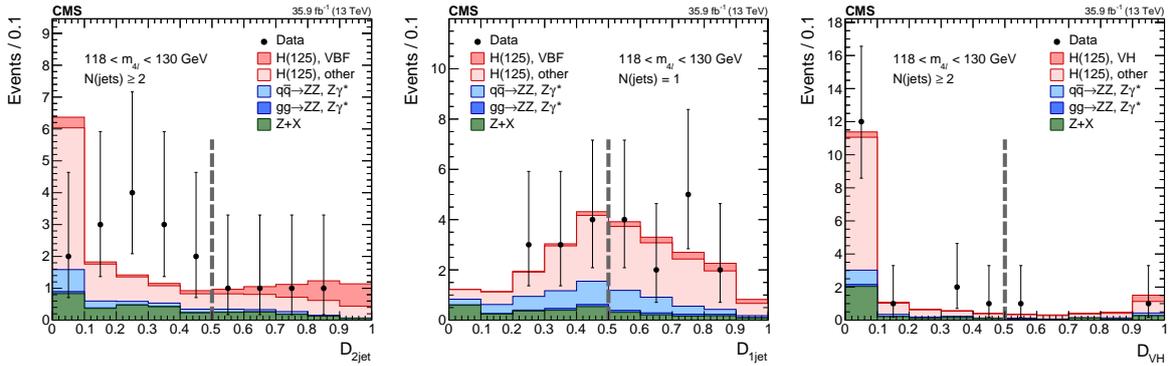

Figure 7: Distribution of categorization discriminants in the mass region $118 < m_{4\ell} < 130\,\mathrm{GeV}$. (Left) $\mathcal{D}_{2\,\mathrm{jet}}$. (Middle) $\mathcal{D}_{1\,\mathrm{jet}}$. (Right) $\mathcal{D}_{\mathrm{VH}} = \max(\mathcal{D}_{\mathrm{WH}}, \mathcal{D}_{\mathrm{ZH}})$. Points with error bars represent the data and stacked histograms represent expected signal and background distributions. The SM Higgs boson signal with $m_{\mathrm{H}} = 125\,\mathrm{GeV}$, denoted as H(125), and the ZZ backgrounds are normalized to the SM expectation, whilst the Z+X background is normalized to the estimation from data. The vertical gray dashed lines denote the working points used in the event categorization. The SM Higgs boson signal is separated into two components: the production mode that is targeted by the specific discriminant, and other production modes, where the gluon fusion dominates. The order in perturbation theory used for the normalization of the irreducible backgrounds is described in Section 7.1.

10.1 Signal strength modifiers

To extract the signal strength modifier we perform a multi-dimensional fit that relies on two variables: the four-lepton invariant mass $m_{4\ell}$ and the $\mathcal{D}_{\text{bkg}}^{\text{kin}}$ discriminant. We define the two-dimensional likelihood function as:

$$\mathcal{L}_{2D}(m_{4\ell}, \mathcal{D}_{\text{bkg}}^{\text{kin}}) = \mathcal{L}(m_{4\ell})\mathcal{L}(\mathcal{D}_{\text{bkg}}^{\text{kin}}|m_{4\ell}). \tag{8}$$

The mass dimension is unbinned and uses the model described in Section 8. The conditional term is implemented by creating a two-dimensional template of $m_{4\ell}$ vs. $\mathcal{D}_{\text{bkg}}^{\text{kin}}$ normalized to 1 for each bin of $m_{4\ell}$. Based on the seven event categories and the three final states (4e, 4μ, 2e2μ), the $(m_{4\ell}, \mathcal{D}_{\text{bkg}}^{\text{kin}})$ unbinned distributions are split into 21 categories.

A simultaneous fit to all categories is performed to extract the signal strength modifier. The relative fraction of 4e, 4μ, and 2e2μ signal events is fixed to the SM prediction. Systematic uncertainties are included in the form of nuisance parameters and the results are obtained using an asymptotic approach with a test statistic based on the profile likelihood ratio [72, 73]. The individual contributions of statistical and systematic uncertainties are separated by performing a likelihood scan removing the systematic uncertainties to determine the statistical uncertainty. The systematic uncertainty is then taken as the difference in quadrature between the total uncertainty and the statistical uncertainty. At the ATLAS and CMS Run 1 combined mass value of $m_{\text{H}} = 125.09$ GeV, the signal strength modifier is $\mu = 1.05 \, ^{+0.15}_{-0.14}$ (stat) $^{+0.11}_{-0.09}$ (syst) $= 1.05^{+0.19}_{-0.17}$. It is compared to the measurement for each of the seven event categories in Fig. 8 (top left). The observed values are consistent with the SM prediction of $\mu = 1$ within the uncertainties. The dominant sources of experimental systematic uncertainty are the uncertainties in the lepton identification efficiencies and integrated luminosity measurement, while the dominant theoretical sources are the uncertainty in the total gluon fusion cross section as well as the uncertainty in the category migration for the gluon fusion process. The contributions to the total uncertainty from experimental and theoretical sources are found to be similar in magnitude.

A fit is performed for five signal strength modifiers (μ_{ggH}, μ_{VBF}, μ_{VHhad}, μ_{VHlep}, and $\mu_{\text{t}\bar{\text{t}}\text{H}}$, all constrained to positive values) that control the contributions of the main SM Higgs boson production modes. The WH and ZH processes are merged, and then split based on the decay of the associated vector boson into either hadronic decays (VHhad) or leptonic decays (VHlep). The results are reported in Fig. 8 (top right) and compared to the expected signal strength modifiers in Table 3. The expected uncertainties are evaluated by generating an Asimov data set [73], which is a representative event sample that provides both the median expectation for an experimental result and its expected statistical variation, in the asymptotic approximation. The coverage of the quoted intervals has been verified for a subset of results using the Feldman-Cousins method [74]. The low observed signal strengths for the VBF, VH, and t$\bar{\text{t}}$H processes can be explained by the mild excess in the untagged category, which leads to a higher than expected signal strength for the gg $\rightarrow$ H process that contributes significantly to the total signal yield in categories that are based on the hadronic activity in the event. In the categories that are not based on hadronic event activity, events with $m_{4\ell}$ near 125 GeV have low $\mathcal{D}_{\text{bkg}}^{\text{kin}}$ values, and are therefore more compatible with the background than the signal hypothesis.

Two signal strength modifiers $\mu_{\text{ggH}, \text{t}\bar{\text{t}}\text{H}}$ and $\mu_{\text{VBF,VH}}$ are introduced as scale factors for the fermion- and vector-boson induced contribution to the expected SM cross section. A two-parameter fit is performed simultaneously to all categories assuming a mass of $m_{\text{H}} = 125.09$ GeV, leading to the measurements of $\mu_{\text{ggH}, \text{t}\bar{\text{t}}\text{H}} = 1.19^{+0.21}_{-0.20}$ and $\mu_{\text{VBF,VH}} = 0.00^{+0.81}_{-0.00}$. The 68% and 95% CL contours in the $(\mu_{\text{ggH}, \text{t}\bar{\text{t}}\text{H}}, \mu_{\text{VBF,VH}})$ plane are shown in Fig. 8 (bottom). The SM predictions of $\mu_{\text{ggH}, \text{t}\bar{\text{t}}\text{H}} = 1$ and $\mu_{\text{VBF,VH}} = 1$ lie within the 68% CL regions of this measurement.
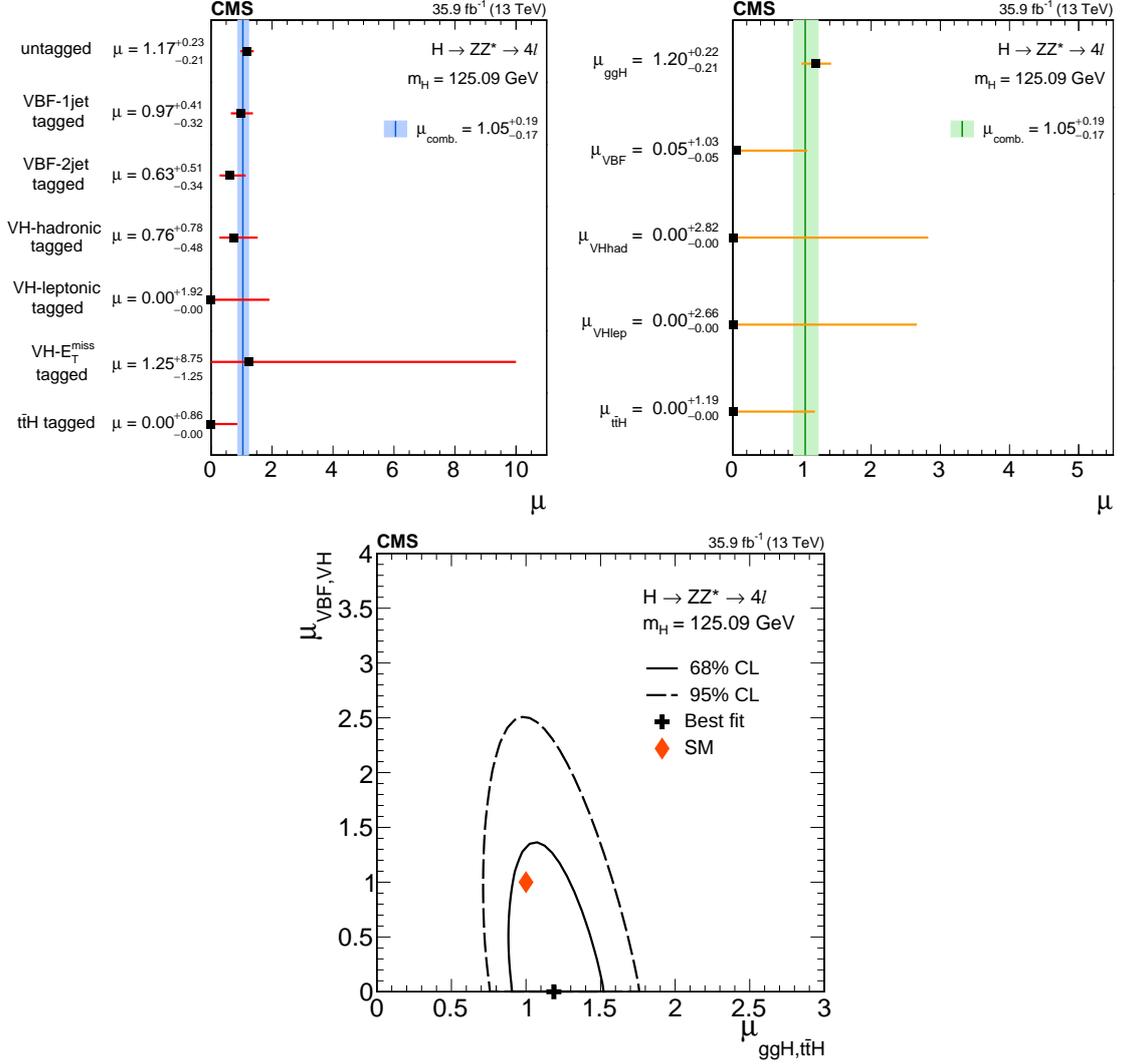
Figure 8: (Top left) Observed values of the signal strength modifier $\mu = \sigma/\sigma_{SM}$ for the seven event categories, compared to the combined μ shown as a vertical line. The horizontal bars and the filled band indicate the $\pm 1\sigma$ uncertainties. (Top right) Results of likelihood scans for the signal strength modifiers corresponding to the main SM Higgs boson production modes, compared to the combined μ shown as a vertical line. The horizontal bars and the filled band indicate the $\pm 1\sigma$ uncertainties. The uncertainties include both statistical and systematic sources. (Bottom) Result of the 2D likelihood scan for the $\mu_{ggH,t\bar{t}H}$ and $\mu_{VBF,VH}$ signal strength modifiers. The solid and dashed contours show the 68% and 95% CL regions, respectively. The cross indicates the best fit values, and the diamond represents the expected values for the SM Higgs boson.

Table 3: Expected and observed signal strength modifiers.

	Inclusive	μ_{ggH}	μ_{VBF}	μ_{VHhad}	μ_{VHlep}	$\mu_{t\bar{t}H}$
Expected	$1.00^{+0.15}_{-0.14}$ (stat)$^{+0.10}_{-0.08}$ (syst)	$1.00^{+0.23}_{-0.21}$	$1.00^{+1.25}_{-0.97}$	$1.00^{+3.96}_{-1.00}$	$1.00^{+3.76}_{-1.00}$	$1.00^{+3.23}_{-1.00}$
Observed	$1.05^{+0.15}_{-0.14}$ (stat)$^{+0.11}_{-0.09}$ (syst)	$1.20^{+0.22}_{-0.21}$	$0.05^{+1.03}_{-0.05}$	$0.00^{+2.83}_{-0.00}$	$0.00^{+2.66}_{-0.00}$	$0.00^{+1.19}_{-0.00}$

10.2   Cross section measurements

In this section we present various measurements of the cross section for Higgs boson production. First we show cross section measurements for five SM Higgs boson production processes (σ_{ggH}, σ_{VBF}, σ_{VHhad}, σ_{VHlep}, and $\sigma_{\text{t}\bar{\text{t}}\text{H}}$) in a simplified fiducial volume defined using a selection on the Higgs boson rapidity $|y_{\text{H}}| < 2.5$. Outside of this volume the analysis has a negligible acceptance. The separation of the production processes is achieved through the categorization of events described in Section 6. This measurement corresponds to the 'stage-0' simplified template cross sections from Ref. [34]. This approach allows one to reduce the dependence of the measurements on the theoretical uncertainties in the SM predictions, avoiding extrapolation of the measurements to the full phase space which carries nontrivial or sizeable theoretical uncertainties. The measured cross sections, normalized to the SM prediction [34], which is denoted as σ_{theo}, are shown in Fig. 9. The dominant sources of experimental systematic uncertainty are the same as in the measurement of the signal strength modifier, while the dominant theoretical source is the uncertainty in the category migration for the gluon fusion process.
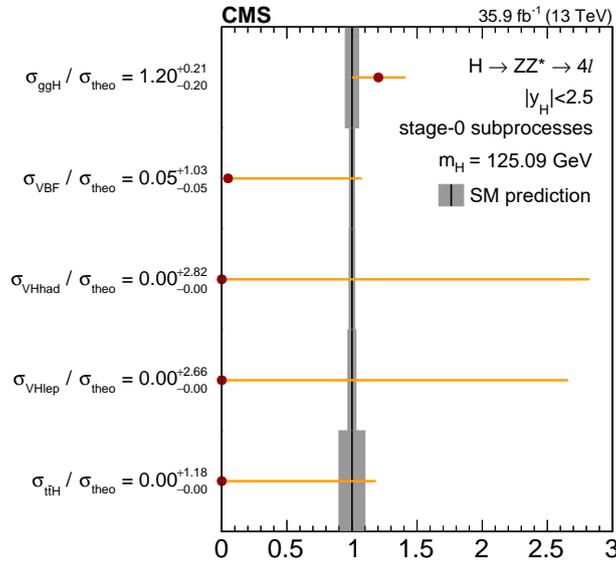
Figure 9: Results of the fit for simplified template cross sections for the 'stage-0 subprocesses', normalized to the SM predictions. The grey bands indicate the theoretical uncertainties in the SM predictions. The orange error bars show the full uncertainty, including experimental uncertainties and theoretical uncertainties causing migration of events between the various categories. See Ref. [34] for further details of this approach.

The cross section for the production and decay $\text{pp} \rightarrow \text{H} \rightarrow 4\ell$ in a tight fiducial phase space is also presented. This measurement has minimal dependence on the assumptions of the relative fraction or kinematic distributions of the separate production modes. The definition of the generator-level fiducial volume, chosen to match closely the reconstruction-level selection, is very similar to the definition used in Ref. [22]. The differences with respect to Ref. [22] are that leptons are defined as "dressed" leptons, as opposed to Born-level leptons, and the lepton isolation criterion is updated to match the reconstruction-level selection. Leptons are "dressed" by adding the four-momenta of photons within $\Delta R < 0.3$ to the bare leptons, and leptons are considered isolated if the scalar sum of transverse momenta of all stable particles, excluding electrons, muons, and neutrinos, within $\Delta R < 0.3$ from the lepton is less than $0.35 p_{\text{T}}$ (GeV). For the measurement of differential cross sections related to jet observables, only well mea-

sured central jets with $p_T > 30\,\text{GeV}$ and $|\eta| < 2.5$ are considered in both the fiducial and reconstruction-level selections. To simplify the definition of the fiducial volume, the $\mathcal{D}_{\text{bkg}}^{\text{kin}}$ discriminant is not used to select the ZZ candidate at the generator level. Instead the Z_1 candidate is chosen to be the one with $m(Z_1)$ closest to the nominal Z boson mass, and in cases where multiple Z_2 candidates satisfy all criteria, the pair of leptons with the highest sum of the transverse momenta is chosen. The same candidate selection is also used at the reconstruction level for the fiducial cross section measurements to align the reconstruction- and fiducial-level selections as closely as possible. The full definition of the fiducial volume is detailed in Table 4 and the acceptance $\mathcal{A}_{\text{fid}}$ for various SM production modes is given in Table 5.

Table 4: Summary of requirements and selections used in the definition of the fiducial phase space for the $\text{pp} \rightarrow \text{H} \rightarrow 4\ell$ cross section measurements.

Lepton kinematics and isolation	
Leading lepton p_T	$p_T > 20\,\text{GeV}$
Subleading lepton p_T	$p_T > 10\,\text{GeV}$
Additional electrons (muons) p_T	$p_T > 7\,(5)\,\text{GeV}$
Pseudorapidity of electrons (muons)	$|\eta| < 2.5\,(2.4)$
Sum p_T of all stable particles within $\Delta R < 0.3$ from lepton	$< 0.35 p_T$
Event topology	
Existence of at least two same-flavor OS lepton pairs, where leptons satisfy criteria above	
Invariant mass of the Z_1 candidate	$40 < m_{Z_1} < 120\,\text{GeV}$
Invariant mass of the Z_2 candidate	$12 < m_{Z_2} < 120\,\text{GeV}$
Distance between selected four leptons	$\Delta R(\ell_i, \ell_j) > 0.02$ for any $i \neq j$
Invariant mass of any opposite-sign lepton pair	$m_{\ell^+\ell'^-} > 4\,\text{GeV}$
Invariant mass of the selected four leptons	$105 < m_{4\ell} < 140\,\text{GeV}$

A maximum likelihood fit of the signal and background parameterizations to the observed 4ℓ mass distribution, $N_{\text{obs}}(m_{4\ell})$, is performed to extract the integrated fiducial cross section σ_{fid} for $\text{pp} \rightarrow \text{H} \rightarrow 4\ell$. The fit is done without any event categorization targeting different production modes and does not use the $\mathcal{D}_{\text{bkg}}^{\text{kin}}$ observable to minimize the model dependence. The fit is performed simultaneously in all final states assuming a Higgs boson mass of $m_H = 125.09\,\text{GeV}$, and the branching fraction of the Higgs boson decays to different final states $(4e, 4\mu, 2e2\mu)$ is allowed to float.

The number of expected events in each final state f and in each bin i of an observable considered is expressed as a function of $m_{4\ell}$ as:

$$
\begin{aligned}
N_{\text{exp}}^{\text{f},i}(m_{4\ell}) &= N_{\text{fid}}^{\text{f},i}(m_{4\ell}) + N_{\text{nonfid}}^{\text{f},i}(m_{4\ell}) + N_{\text{nonres}}^{\text{f},i}(m_{4\ell}) + N_{\text{bkg}}^{\text{f},i}(m_{4\ell}) \\
&= \sum_j \epsilon_{i,j}^{\text{f}} \left(1 + f_{\text{nonfid}}^{\text{f},i} \right) \sigma_{\text{fid}}^{\text{f},j} \mathcal{L} \, \mathcal{P}_{\text{res}}(m_{4\ell}) \\
&\quad + N_{\text{nonres}}^{\text{f},i} \mathcal{P}_{\text{nonres}}(m_{4\ell}) + N_{\text{bkg}}^{\text{f},i} \mathcal{P}_{\text{bkg}}(m_{4\ell}).
\end{aligned}
\tag{9}
$$

The shape of the resonant signal contribution, $\mathcal{P}_{\text{res}}(m_{4\ell})$, is modelled by a double-sided Crystal Ball function, as described in Section 8, and the normalization is proportional to the fiducial cross section. The non-resonant contribution from WH, ZH, and $\text{t}\bar{\text{t}}\text{H}$ production, N_{nonres}, is modeled by a Landau distribution, $\mathcal{P}_{\text{nonres}}(m_{4\ell})$, whose shape parameters are constrained in the fit to be within a range determined from signal samples with full detector simulation and is treated as a background in this measurement.

The $\epsilon^{\mathrm{f}}_{i,j}$ factor represents the detector response matrix that maps the number of expected events in a given observable bin j at the fiducial level to the number of expected events in the bin i at the reconstruction level. This response matrix is measured using signal samples with full detector simulation and corrected for residual differences between data and simulation. This procedure accounts for the unfolding of detector effects from the observed distributions and is the same as in Refs. [75] and [22]. In the case of the integrated fiducial cross section measurement the efficiencies reduce to single values, which for different SM production modes are listed in Table 5.

An additional resonant contribution arises from events which are reconstructed, but do not originate from the fiducial phase space, N_{nonfid}. These events are due to detector effects that cause differences between the quantities used for the fiducial phase space definition and the analogous quantities at the reconstruction level. This contribution is treated as background and is referred to as the "nonfiducial signal" contribution. The shape of these events is verified using signal samples with full detector simulation to be identical to the shape of the fiducial signal, and its normalization is fixed to be a fraction of the fiducial signal component. The value of this fraction, which we denote as f_{nonfid}, has been determined from signal samples with full detector simulation for each of the signal production modes studied. The value of f_{nonfid} for different signal production modes is shown in Table 5.

Table 5: Summary of the fraction of signal events for different SM signal production modes within the fiducial phase space (acceptance $\mathcal{A}_{\mathrm{fid}}$), reconstruction efficiency (ϵ) for signal events from within the fiducial phase space, and ratio of reconstructed events which are from outside the fiducial phase space to reconstructed events which are from within the fiducial phase space (f_{nonfid}). For all production modes the values given are for $m_{\mathrm{H}} = 125\,\mathrm{GeV}$. Also shown in the last column is the factor $(1 + f_{\mathrm{nonfid}})\epsilon$ which regulates the signal yield for a given fiducial cross section, as shown in Eq. 9. The uncertainties listed are statistical only. The theoretical uncertainty in $\mathcal{A}_{\mathrm{fid}}$ for the SM is less than 1%.

Signal process	$\mathcal{A}_{\mathrm{fid}}$	ϵ	f_{nonfid}	$(1 + f_{\mathrm{nonfid}})\epsilon$
gg→H (POWHEG)	0.398 ± 0.001	0.592 ± 0.001	0.049 ± 0.001	0.621 ± 0.001
VBF (POWHEG)	0.445 ± 0.001	0.601 ± 0.002	0.038 ± 0.001	0.624 ± 0.002
WH (POWHEG MINLO)	0.314 ± 0.001	0.577 ± 0.002	0.068 ± 0.001	0.616 ± 0.002
ZH (POWHEG MINLO)	0.342 ± 0.002	0.592 ± 0.003	0.071 ± 0.002	0.634 ± 0.003
ttH (POWHEG)	0.311 ± 0.002	0.572 ± 0.003	0.136 ± 0.003	0.650 ± 0.004

The results are compared to the predictions obtained from POWHEG and NNLOPS [76] which have NLO and NNLO accuracy in pQCD for inclusive distributions, respectively. In both cases the total gluon fusion cross section is taken from Ref. [35].

The integrated fiducial cross section is measured to be $\sigma_{\mathrm{fid}} = 2.92\,^{+0.48}_{-0.44}\,(\mathrm{stat})\,^{+0.28}_{-0.24}\,(\mathrm{syst})$ fb. This can be compared to the SM expectation obtained from NNLOPS of $\sigma^{\mathrm{SM}}_{\mathrm{fid}} = 2.76 \pm 0.14$ fb. The integrated fiducial cross section as a function of $\sqrt{s}$ is also shown in Fig. 10. The compatibility of the integrated fiducial cross sections measured in the 4e, 4μ, and 2e2μ final states with the SM prediction is estimated using a likelihood ratio with the three cross sections at their best fit values in the numerator and the three cross sections fixed to the SM predictions in the denominator. The compatibility, defined as the asymptotic p-value of the fit, is found to be 88%. The measured differential cross section results for $p_{\mathrm{T}}(\mathrm{H})$, N(jets), and $p_{\mathrm{T}}(\mathrm{jet})$ of the leading associated jet can also be seen in Fig. 10. The dominant sources of systematic uncertainty are the experimental uncertainties in the lepton identification efficiencies and integrated luminosity measurement, and the theoretical sources of uncertainty are found to be subdominant. To estimate the model dependence of the measurement, the unfolding procedure is repeated us-

ing different response matrices created by varying the relative fraction of each SM production mode within its experimental constraints. The uncertainty is determined to be negligible with respect to the experimental systematic uncertainties.
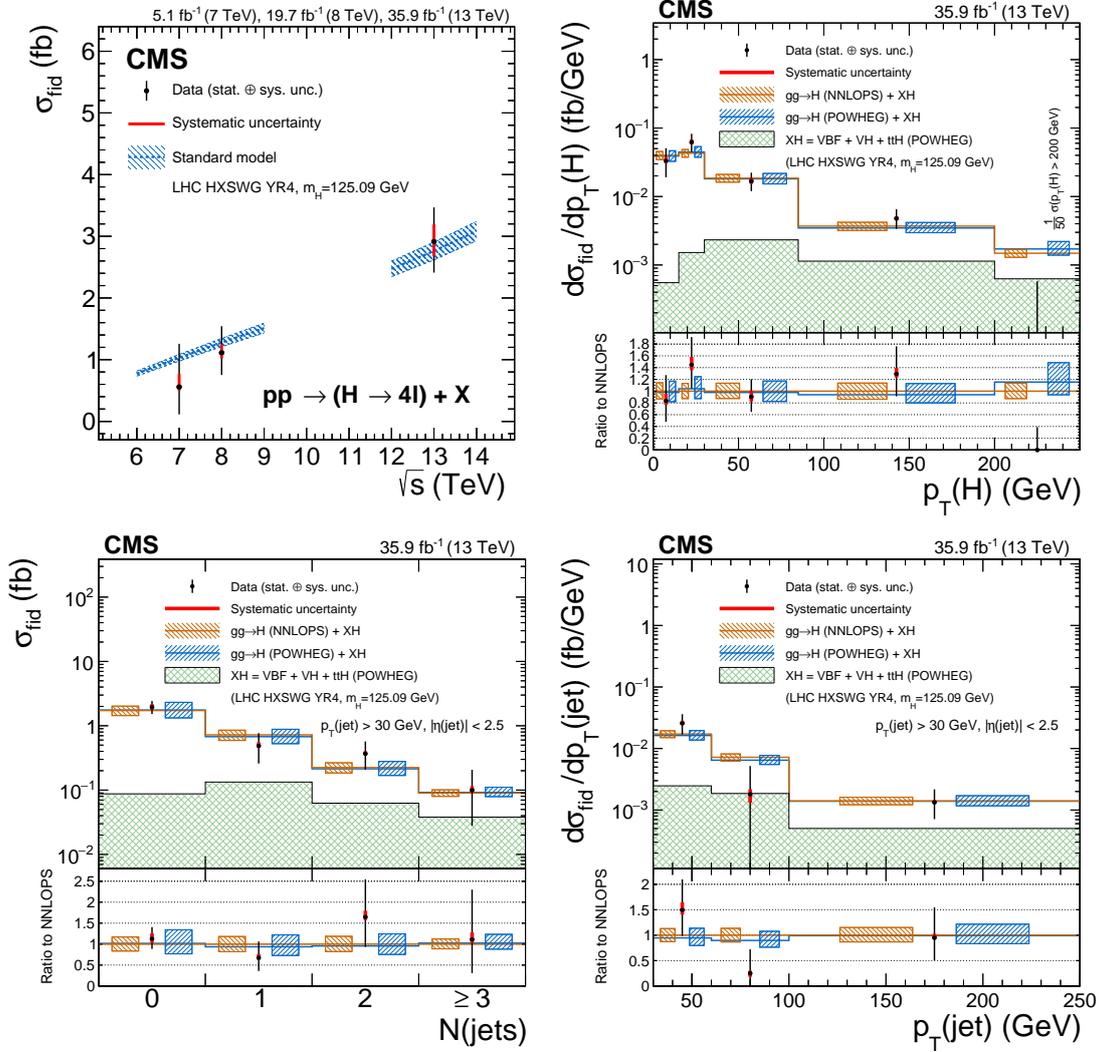

Figure 10: The measured fiducial cross section as a function of $\sqrt{s}$ (top left). The acceptance is calculated using NNLOPS at $\sqrt{s} = 13\,\text{TeV}$ and HRES [39, 40] at $\sqrt{s} = 7$ and 8 TeV and the total cross sections and uncertainties are taken from Ref. [34]. The fiducial volume for $\sqrt{s} = 7$ and 8 TeV uses the lepton isolation definition from Ref. [22], while for $\sqrt{s} = 13\,\text{TeV}$ the definition described in the text is used. The results of the differential cross section measurements are shown for $p_T(H)$ (top right), N(jets) (bottom left) and $p_T(\text{jet})$ of the leading associated jet (bottom right). The acceptance and theoretical uncertainties in the differential bins are calculated using POWHEG and NNLOPS. The subdominant component of the signal (VBF + VH + t$\bar{\text{t}}$H) is denoted as XH. In the differential cross section measurement for $p_T(H)$, the last bin represents the integrated cross section for $p_T(H) > 200\,\text{GeV}$ and is scaled by 1/50 for presentation purposes. No events are observed with $p_T(H) > 200\,\text{GeV}$.

10.3 Higgs boson mass measurement

In this section we show the results of the measurement of the mass of the resonance, using additional information in the likelihood fit with respect to the signal strength and cross section measurements.

To improve the four-lepton invariant mass resolution, a kinematic fit is performed using a mass constraint on the intermediate Z resonance. Previous studies [14] of the Higgs boson mass show that the selected Z_1 has a significant on-shell component, while the invariant mass distribution for the selected Z_2 is wider than the detector resolution. Therefore only the Z_1 candidate is considered when performing the kinematic constraint.

The likelihood to be maximized is constructed as follows:

$$\mathcal{L}(\hat{p}_T^1, \hat{p}_T^2 | p_T^1, \sigma_{p_T^1}, p_T^2, \sigma_{p_T^2}) = \text{Gauss}(p_T^1 | \hat{p}_T^1, \sigma_{p_T^1}) \, \text{Gauss}(p_T^2 | \hat{p}_T^2, \sigma_{p_T^2}) \, \mathcal{L}(m_{12} | m_Z, m_H), \quad (10)$$

where p_T^1 and a^2 are the reconstructed transverse momenta of the two leptons forming the Z_1 candidate, $\sigma_{p_T^1}$ and $\sigma_{p_T^2}$ are the corresponding per-lepton resolutions, $\hat{p}_T^1$ and $\hat{p}_T^2$ are the refitted transverse momenta, and m_{12} is the invariant mass calculated from the refitted four-momenta. The term $\mathcal{L}(m_{12} | m_Z, m_H)$ is the mass constraint term. For a Higgs boson mass near 125 GeV, the selected Z_1 is not always on-shell, so a Breit–Wigner shape does not perfectly describe the Z_1 shape at the generator level. We therefore choose $\mathcal{L}(m_{12} | m_Z, m_H)$ to be the $m(Z_1)$ shape at the generator level from the SM Higgs boson sample with $m_H = 125$ GeV, where the same algorithm for selecting the Z_1 and Z_2 candidates, as described in Section 4, is used. For each event, the likelihood is maximized and the refitted transverse momenta are used to recalculate the four-lepton mass and mass uncertainty, which are denoted as $m_{4\ell}'$ and $\mathcal{D}_{mass}'$, respectively. These distributions are then used to build the likelihood used to extract the Higgs boson mass.

The 1D likelihood scans vs. m_H, while profiling the signal strength modifier μ along with all other nuisance parameters for the 1D $\mathcal{L}(m_{4\ell}')$, 2D $\mathcal{L}(m_{4\ell}', \mathcal{D}_{mass}')$, and 3D $\mathcal{L}(m_{4\ell}', \mathcal{D}_{mass}', \mathcal{D}_{bkg}^{kin})$ fits, including the $m(Z_1)$ constraint, are shown in Fig. 11. All systematic uncertainties described in Section 9 are included. When estimating separately the systematic and statistical uncertainties, the signal strength is profiled in the likelihood scan with the systematic uncertainties removed, so that its uncertainty is included in the statistical uncertainty. As in the measurement of the signal strengths, the relative fraction of 4e, 4μ, and 2e2μ signal events is fixed to the SM prediction. If the relative fractions are allowed to float, the change in the fitted mass value is much smaller than the uncertainty.

The best fit masses and the expected increase in the uncertainty relative to the 3D fit with the $m(Z_1)$ constraint for each of the six fits are shown in Table 6. The nominal result for the mass measurement is obtained from the 3D fit with the $m(Z_1)$ constraint, for which the fitted value of m_H in the three subchannels is $m_H^{4\mu} = 124.94 \pm 0.25\,(\text{stat}) \pm 0.08\,(\text{syst})\,\text{GeV}$, $m_H^{4e} = 124.37 \pm 0.62\,(\text{stat}) \pm 0.38\,(\text{syst})\,\text{GeV}$, and $m_H^{2e2\mu} = 125.95 \pm 0.32\,(\text{stat}) \pm 0.14\,(\text{syst})\,\text{GeV}$ leading to a combined value $m_H = 125.26 \pm 0.20\,(\text{stat}) \pm 0.08\,(\text{syst})\,\text{GeV}$. The systematic uncertainty in the mass measurement is completely dominated by the uncertainty in the lepton momentum scale. The expected uncertainty in the mass measurement using the 3D fit with the $m(Z_1)$ constraint is evaluated with two Asimov data sets. The "prefit" expected uncertainty is $\pm 0.24\,(\text{stat}) \pm 0.09\,(\text{syst})\,\text{GeV}$. Here $m_H = 125$ GeV, $\mu = 1$, and all nuisance parameters are fixed to their nominal values. The "postfit" expected uncertainty with m_H, μ, and all nuisance parameters fixed to their best-fit estimates from the data is $\pm 0.23\,(\text{stat}) \pm 0.08\,(\text{syst})\,\text{GeV}$. The probability of the "prefit" uncertainty being less than or equal to the observed value is determined from an ensemble of pseudo-experiments to be about 18%. The mutual compat-

ibility of the m_H results from the three individual channels is tested using a likelihood ratio with three masses in the numerator and a common mass in the denominator, and thus two degrees of freedom. The signal strength is profiled in both the numerator and denominator. The resulting compatibility, defined as the asymptotic p-value of the fit, is 2.5%. The tension between the three individual channels is driven by the difference between the 4μ and $2e2\mu$ channels, where the compatibility of the 1D mass measurements without the $m(Z_1)$ constraint is 8%. In the 1D mass measurement the main potential source of systematic bias is the lepton momentum scale; this possibility is disfavored by the fact that the measured mass in the $2e2\mu$ channel is not in between the measurements in the 4e and 4μ channels. This bias has also been checked by performing the 1D mass measurements without the $m(Z_1)$ constraint using $Z \to 4\ell$ events, and the resulting mass is measured to be $m_Z^{4\mu} = 90.85 \pm 0.27\,(\text{stat}) \pm 0.04\,(\text{syst})\,\text{GeV}$, $m_Z^{4e} = 90.85 \pm 0.74\,(\text{stat}) \pm 0.28\,(\text{syst})\,\text{GeV}$, and $m_Z^{2e2\mu} = 90.61 \pm 0.48\,(\text{stat}) \pm 0.10\,(\text{syst})\,\text{GeV}$ leading to a combined value $m_Z = 90.84 \pm 0.23\,(\text{stat}) \pm 0.07\,(\text{syst})\,\text{GeV}$. The compatibility with the nominal Z-boson mass from Ref. [57] is 14% and the mutual compatibility between the three individual channels is 90%. The modelling of the event-by-event mass uncertainties is a possible source of systematic bias in the 2D and 3D measurements. It is checked by performing a Kolmogorov-Smirnov compatibility test of the expected and observed distributions in an expanded $m_{4\ell}$ range yielding p-values of 10% for the $2e2\mu$ channel, 55% for the 4e channel, and 94% for the 4μ channel.
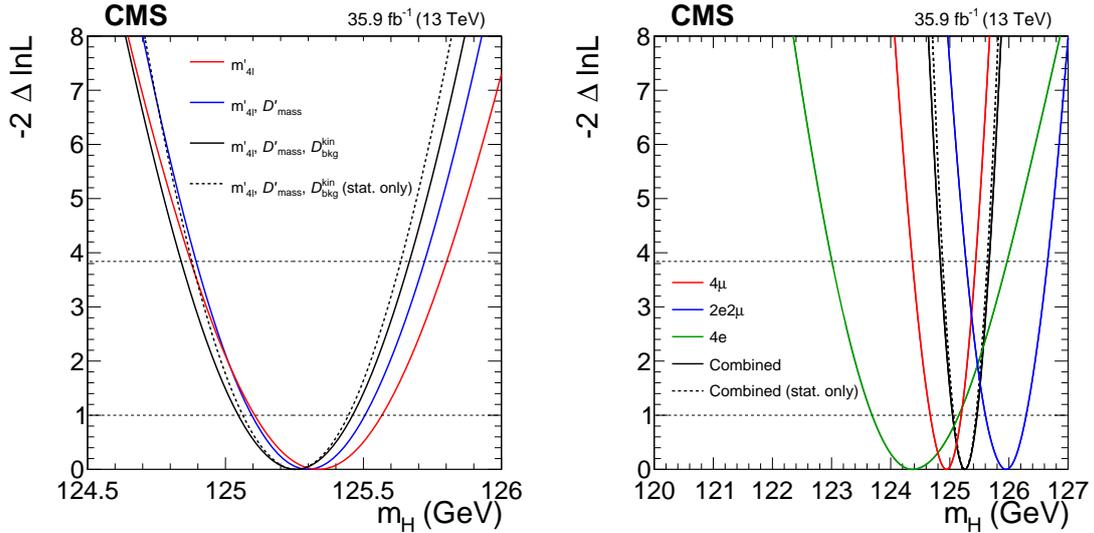
Figure 11: Left: 1D likelihood scans as a function of the Higgs boson mass for the 1D, 2D, and 3D measurement. Right: 1D likelihood scans as a function of mass for the different final states and the combination of all final states for the 3D mass measurement. The likelihood scans are shown for the mass measurement using the refitted mass distribution with the $m(Z_1)$ constraint. Solid lines represent scans with all uncertainties included, dashed lines those with only statistical uncertainties.

Table 6: Best fit values for the mass of the Higgs boson measured in the 4ℓ final states, with the 1D, 2D, and 3D fit, respectively, as described in the text. All mass values are given in GeV. The uncertainties include both the statistical and systematic components. The expected m_{H} uncertainty change shows the change in the expected precision on the measurement for the different fit scenarios, relative to 3D $\mathcal{L}(m'_{4\ell}, \mathcal{D}'_{\mathrm{mass}}, \mathcal{D}^{\mathrm{kin}}_{\mathrm{bkg}})$.

No $m(Z_1)$ constraint	3D: $\mathcal{L}(m_{4\ell}, \mathcal{D}_{\mathrm{mass}}, \mathcal{D}^{\mathrm{kin}}_{\mathrm{bkg}})$	2D: $\mathcal{L}(m_{4\ell}, \mathcal{D}_{\mathrm{mass}})$	1D: $\mathcal{L}(m_{4\ell})$
Expected m_{H} uncertainty change	+8.1%	+11%	+21%
Observed m_{H} (GeV)	125.28±0.22	125.36±0.24	125.39±0.25
With $m(Z_1)$ constraint	3D: $\mathcal{L}(m'_{4\ell}, \mathcal{D}'_{\mathrm{mass}}, \mathcal{D}^{\mathrm{kin}}_{\mathrm{bkg}})$	2D: $\mathcal{L}(m'_{4\ell}, \mathcal{D}'_{\mathrm{mass}})$	1D: $\mathcal{L}(m'_{4\ell})$
Expected m_{H} uncertainty change	—	+3.2%	+11%
Observed m_{H} (GeV)	125.26±0.21	125.30±0.21	125.34±0.23

10.4   Measurement of the Higgs boson width using on-shell production

In this section, we describe a model-independent measurement of the width performed using the $m_{4\ell}$ distribution in the range $105 < m_{4\ell} < 140\,\text{GeV}$. This measurement is limited by the four-lepton invariant mass resolution and is therefore sensitive to a width of about $1\,\text{GeV}$. Therefore, we take into account the interference between the signal and background production of the 4ℓ final state in this analysis.

An unbinned maximum likelihood fit to the $m_{4\ell}$ distribution is performed. The strengths of fermion and vector boson induced couplings are independent and are left unconstrained in the fit. By splitting events into two categories, namely those with a VBF-like two-jet topology and the rest, it is possible to constrain the two sets of couplings. The general parameterization of the probability density function is described in Section 8.

The joint constraint on the width Γ_H and mass m_H of the Higgs boson is shown in Fig. 12 (left). Figure 12 (right) shows the likelihood as a function of Γ_H with the m_H parameter unconstrained. The width is constrained to be $\Gamma_H < 1.10\,\text{GeV}$ at 95% CL. The observed and expected results are summarized in Table 7 and are consistent with the expected detector resolution. The dominant sources of uncertainty are the uncertainty in the lepton momentum scale when determining the mass and the uncertainty in the four-lepton mass resolution when determining the width.
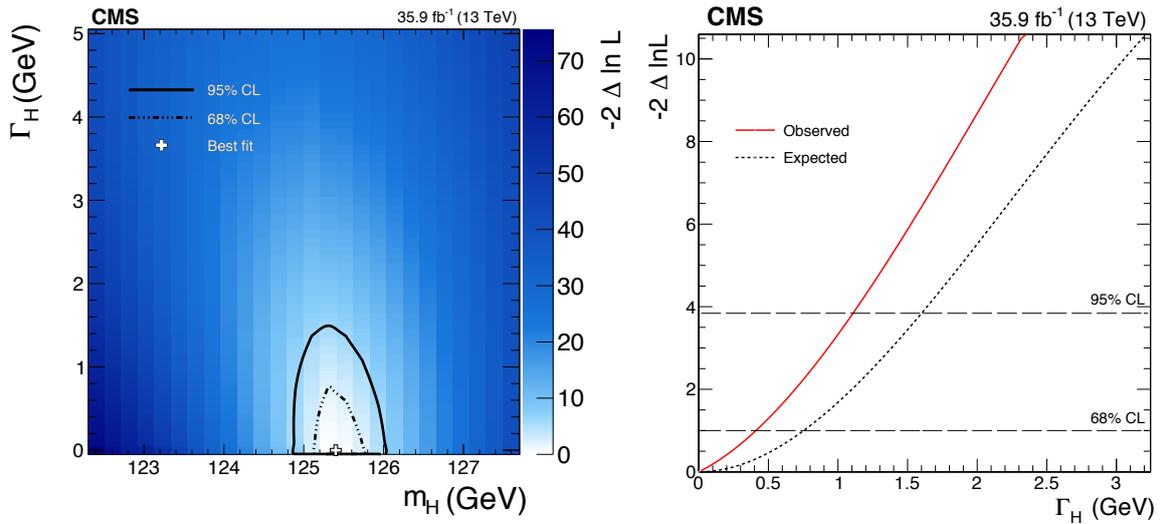
Figure 12: (Left) Observed likelihood scan of m_H and Γ_H using the signal range $105 < m_{4\ell} < 140\,\text{GeV}$. (Right) Observed and expected likelihood scan of Γ_H using the signal range $105 < m_{4\ell} < 140\,\text{GeV}$, with m_H profiled.

Table 7: Summary of allowed 68% CL (central values with uncertainties) and 95% CL (ranges in square brackets) intervals on the width Γ_H of the Higgs boson. The expected results are quoted for the SM signal production cross section ($\mu_{\text{VBF,VH}} = \mu_{\text{ggH,t}\bar{\text{t}}\text{H}} = 1$) and the values of $m_H = 125\,\text{GeV}$. In the observed results $\mu_{\text{VBF,VH}}$ and $\mu_{\text{ggH,t}\bar{\text{t}}\text{H}}$ are left unconstrained in the fit.

Parameter	$m_{4\ell}$ range	Expected	Observed
Γ_H (GeV)	$[105, 140]$	$0.00^{+0.75}_{-0.00}$ $[0.00, 1.60]$	$0.00^{+0.41}_{-0.00}$ $[0.00, 1.10]$

11 Summary

The first results on Higgs boson production in the four-lepton final state at $\sqrt{s} = 13\,\text{TeV}$ have been presented, using $35.9\,\text{fb}^{-1}$ of pp collisions collected by the CMS experiment at the LHC. The signal strength modifier μ, defined as the ratio of the observed Higgs boson rate in the $\text{H} \rightarrow \text{ZZ} \rightarrow 4\ell$ decay channel to the standard model expectation, is measured to be $\mu = 1.05\,^{+0.15}_{-0.14}\,(\text{stat})\,^{+0.11}_{-0.09}\,(\text{syst}) = 1.05^{+0.19}_{-0.17}$ at $m_\text{H} = 125.09\,\text{GeV}$, the combined ATLAS and CMS measurement of the Higgs boson mass. Two signal strength modifiers associated with the fermion- and vector-boson induced contributions to the expected standard model cross section are measured to be $\mu_{\text{ggH},\text{t}\bar{\text{t}}\text{H}} = 1.19^{+0.21}_{-0.20}$ and $\mu_{\text{VBF},\text{VH}} = 0.00^{+0.81}_{-0.00}$, respectively. The cross section at $\sqrt{s} = 13\,\text{TeV}$ in a fiducial phase space defined to match the experimental acceptance in terms of the lepton kinematics and event topology, predicted in the standard model to be $2.76 \pm 0.14\,\text{fb}$, is measured to be $2.92\,^{+0.48}_{-0.44}\,(\text{stat})\,^{+0.28}_{-0.24}\,(\text{syst})\,\text{fb}$. Differential cross sections are reported as a function of the transverse momentum of the Higgs boson, the number of associated jets, and the transverse momentum of the leading associated jet. The mass is measured to be $m_\text{H} = 125.26 \pm 0.20\,(\text{stat}) \pm 0.08\,(\text{syst})\,\text{GeV}$ and the width is constrained to be $\Gamma_\text{H} < 1.10\,\text{GeV}$ at 95% confidence level. The production and decay properties of the Higgs boson are consistent, within their uncertainties, with the expectations for the standard model Higgs boson.

Acknowledgments

References

[1] ATLAS Collaboration, "Observation of a new particle in the search for the Standard Model Higgs boson with the ATLAS detector at the LHC", *Phys. Lett. B* **716** (2012) 1, `doi:10.1016/j.physletb.2012.08.020`, `arXiv:1207.7214`.

[2] CMS Collaboration, "Observation of a new boson at a mass of 125 GeV with the CMS experiment at the LHC", *Phys. Lett. B* **716** (2012) 30, `doi:10.1016/j.physletb.2012.08.021`, `arXiv:1207.7235`.

[3] CMS Collaboration, "Observation of a new boson with mass near 125 GeV in pp collisions at $\sqrt{s}$ = 7 and 8 TeV", *JHEP* **06** (2013) 081, `doi:10.1007/JHEP06(2013)081`, `arXiv:1303.4571`.

[4] CMS Collaboration, "Precise determination of the mass of the Higgs boson and tests of compatibility of its couplings with the standard model predictions using proton

collisions at 7 and 8 TeV", *Eur. Phys. J. C* **75** (2015) 212,
doi:10.1140/epjc/s10052-015-3351-7, arXiv:1412.8662.

[5] ATLAS Collaboration, "Measurements of the Higgs boson production and decay rates and coupling strengths using *pp* collision data at $\sqrt{s} = 7$ and 8 TeV in the ATLAS experiment", *Eur. Phys. J. C* **76** (2016) 6, doi:10.1140/epjc/s10052-015-3769-y, arXiv:1507.04548.

[6] ATLAS and CMS Collaborations, "Measurements of the Higgs boson production and decay rates and constraints on its couplings from a combined ATLAS and CMS analysis of the LHC pp collision data at $\sqrt{s} = 7$ and 8 TeV", *JHEP* **08** (2016) 45, doi:10.1007/JHEP08(2016)045, arXiv:1606.02266.

[7] F. Englert and R. Brout, "Broken symmetry and the mass of gauge vector mesons", *Phys. Rev. Lett.* **13** (1964) 321, doi:10.1103/PhysRevLett.13.321.

[8] P. W. Higgs, "Broken symmetries, massless particles and gauge fields", *Phys. Lett.* **12** (1964) 132, doi:10.1016/0031-9163(64)91136-9.

[9] P. W. Higgs, "Broken symmetries and the masses of gauge bosons", *Phys. Rev. Lett.* **13** (1964) 508, doi:10.1103/PhysRevLett.13.508.

[10] G. S. Guralnik, C. R. Hagen, and T. W. B. Kibble, "Global conservation laws and massless particles", *Phys. Rev. Lett.* **13** (1964) 585, doi:10.1103/PhysRevLett.13.585.

[11] P. W. Higgs, "Spontaneous symmetry breakdown without massless bosons", *Phys. Rev.* **145** (1966) 1156, doi:10.1103/PhysRev.145.1156.

[12] T. W. B. Kibble, "Symmetry breaking in non-abelian gauge theories", *Phys. Rev.* **155** (1967) 1554, doi:10.1103/PhysRev.155.1554.

[13] ATLAS and CMS Collaborations, "Combined measurement of the Higgs boson mass in *pp* collisions at $\sqrt{s} = 7$ and 8 TeV with the ATLAS and CMS experiments", *Phys. Rev. Lett.* **114** (2015) 191803, doi:10.1103/PhysRevLett.114.191803, arXiv:1503.07589.

[14] CMS Collaboration, "Measurement of the properties of a Higgs boson in the four-lepton final state", *Phys. Rev. D* **89** (2014) 092007, doi:10.1103/PhysRevD.89.092007, arXiv:1312.5353.

[15] CMS Collaboration, "Study of the mass and spin-parity of the Higgs boson candidate via its decays to *Z* boson pairs", *Phys. Rev. Lett.* **110** (2013) 081803, doi:10.1103/PhysRevLett.110.081803, arXiv:1212.6639.

[16] CMS Collaboration, "Constraints on the spin-parity and anomalous HVV couplings of the Higgs boson in proton collisions at 7 and 8 TeV", *Phys. Rev. D* **92** (2015) 012004, doi:10.1103/PhysRevD.92.012004, arXiv:1411.3441.

[17] ATLAS Collaboration, "Measurements of Higgs boson production and couplings in the four-lepton channel in pp collisions at center-of-mass energies of 7 and 8 TeV with the ATLAS detector", *Phys. Rev. D* **91** (2015) 012006, doi:10.1103/PhysRevD.91.012006, arXiv:1408.5191.

[18] ATLAS Collaboration, "Study of the spin and parity of the Higgs boson in diboson decays with the ATLAS detector", *Eur. Phys. J. C* **75** (2015) 476, `doi:10.1140/epjc/s10052-015-3685-1`, `arXiv:1506.05669`. [Erratum: `doi:10.1140/epjc/s10052-016-3934-y`].

[19] CMS Collaboration, "Constraints on the Higgs boson width from off-shell production and decay to Z-boson pairs", *Phys. Lett. B* **736** (2014) 64, `doi:10.1016/j.physletb.2014.06.077`, `arXiv:1405.3455`.

[20] CMS Collaboration, "Limits on the Higgs boson lifetime and width from its decay to four charged leptons", *Phys. Rev. D* **92** (2015) 072010, `doi:10.1103/PhysRevD.92.072010`, `arXiv:1507.06656`.

[21] ATLAS Collaboration, "Constraints on the off-shell Higgs boson signal strength in the high-mass ZZ and WW final states with the ATLAS detector", *Eur. Phys. J. C* **75** (2015) 335, `doi:10.1140/epjc/s10052-015-3542-2`, `arXiv:1503.01060`.

[22] CMS Collaboration, "Measurement of differential and integrated fiducial cross sections for Higgs boson production in the four-lepton decay channel in pp collisions at $\sqrt{s} = 7$ and 8 TeV", *JHEP* **04** (2016) 005, `doi:10.1007/JHEP04(2016)005`, `arXiv:1512.08377`.

[23] ATLAS Collaboration, "Measurements of the total and differential Higgs boson production cross sections combining the $H \to \gamma\gamma$ and $H \to ZZ^* \to 4l$ decay channels at $\sqrt{s} = 8$ TeV with the ATLAS detector", *Phys. Rev. Lett.* **115** (2015) 091801, `doi:10.1103/PhysRevLett.115.091801`, `arXiv:1504.05833`.

[24] CMS Collaboration, "The CMS experiment at the CERN LHC", *JINST* **3** (2008) S08004, `doi:10.1088/1748-0221/3/08/S08004`.

[25] CMS Collaboration, "Description and performance of track and primary-vertex reconstruction with the CMS tracker", *JINST* **9** (2014) P10009, `doi:10.1088/1748-0221/9/10/P10009`, `arXiv:1405.6569`.

[26] CMS Collaboration, "Performance of electron reconstruction and selection with the CMS detector in proton-proton collisions at $\sqrt{s} = 8$ TeV", *JINST* **10** (2015) P06005, `doi:10.1088/1748-0221/10/06/P06005`, `arXiv:1502.02701`.

[27] CMS Collaboration, "Performance of CMS muon reconstruction in pp collision events at $\sqrt{s} = 7$ TeV", *JINST* **7** (2012) P10002, `doi:10.1088/1748-0221/7/10/P10002`, `arXiv:1206.4071`.

[28] CMS Collaboration, "The CMS trigger system", *JINST* **12** (2017) P01020, `doi:10.1088/1748-0221/12/01/P01020`, `arXiv:1609.02366`.

[29] CMS Collaboration, "Measurement of the inclusive W and Z production cross sections in pp collisions at $\sqrt{s} = 7$ TeV", *JHEP* **10** (2011) 132, `doi:10.1007/JHEP10(2011)132`, `arXiv:1107.4789`.

[30] S. Alioli, P. Nason, C. Oleari, and E. Re, "NLO vector-boson production matched with shower in POWHEG", *JHEP* **07** (2008) 060, `doi:10.1088/1126-6708/2008/07/060`, `arXiv:0805.4802`.

[31] P. Nason, "A new method for combining NLO QCD with shower Monte Carlo algorithms", *JHEP* **11** (2004) 040, `doi:10.1088/1126-6708/2004/11/040`, `arXiv:hep-ph/0409146`.

[32] S. Frixione, P. Nason, and C. Oleari, "Matching NLO QCD computations with parton shower simulations: the POWHEG method", *JHEP* **11** (2007) 070, `doi:10.1088/1126-6708/2007/11/070`, `arXiv:0709.2092`.

[33] G. Luisoni, P. Nason, C. Oleari, and F. Tramontano, "HW$^\pm$/HZ + 0 and 1 jet at NLO with the POWHEG BOX interfaced to GoSam and their merging within MiNLO", *JHEP* **10** (2013) 1, `doi:10.1007/JHEP10(2013)083`, `arXiv:1306.2542`.

[34] D. de Florian et al., "Handbook of LHC Higgs cross sections: 4. deciphering the nature of the Higgs sector", CERN Report CERN-2017-002-M, 2016. `doi:10.23731/CYRM-2017-002`, `arXiv:1610.07922`.

[35] C. Anastasiou et al., "High precision determination of the gluon fusion Higgs boson cross-section at the LHC", *JHEP* **05** (2016) 058, `doi:10.1007/JHEP05(2016)058`, `arXiv:1602.00695`.

[36] R. D. Ball et al., "Unbiased global determination of parton distributions and their uncertainties at NNLO and at LO", *Nucl. Phys. B* **855** (2012) 153, `doi:10.1016/j.nuclphysb.2011.09.024`, `arXiv:1107.2652`.

[37] Y. Gao et al., "Spin determination of single-produced resonances at hadron colliders", *Phys. Rev. D* **81** (2010) 075022, `doi:10.1103/PhysRevD.81.075022`, `arXiv:1001.3396`. [Erratum: `doi:10.1103/PhysRevD.81.079905`].

[38] S. Bolognesi et al., "On the spin and parity of a single-produced resonance at the LHC", *Phys. Rev. D* **86** (2012) 095031, `doi:10.1103/PhysRevD.86.095031`, `arXiv:1208.4018`.

[39] D. de Florian, G. Ferrera, M. Grazzini, and D. Tommasini, "Higgs boson production at the LHC: transverse momentum resummation effects in the $H \to \gamma\gamma$, $H \to WW \to \ell\nu\ell\nu$ and $H \to ZZ \to 4\ell$ decay modes", *JHEP* **06** (2012) 132, `doi:10.1007/JHEP06(2012)132`, `arXiv:1203.6321`.

[40] M. Grazzini and H. Sargsyan, "Heavy-quark mass effects in Higgs boson production at the LHC", *JHEP* **09** (2013) 129, `doi:10.1007/JHEP09(2013)129`, `arXiv:1306.4581`.

[41] J. M. Campbell and R. K. Ellis, "MCFM for the Tevatron and the LHC", *Nucl. Phys. Proc. Suppl.* **205** (2010) 10, `doi:10.1016/j.nuclphysbps.2010.08.011`, `arXiv:1007.3492`.

[42] T. Sjöstrand et al., "An introduction to PYTHIA 8.2", *Comput. Phys. Commun.* **191** (2015) 159, `doi:10.1016/j.cpc.2015.01.024`, `arXiv:1410.3012`.

[43] CMS Collaboration, "Event generator tunes obtained from underlying event and multiparton scattering measurements", *Eur. Phys. J. C* **76** (2016) 155, `doi:10.1140/epjc/s10052-016-3988-x`, `arXiv:1512.00815`.

[44] GEANT4 Collaboration, "GEANT4—a simulation toolkit", *Nucl. Instrum. Meth. A* **506** (2003) 250, `doi:10.1016/S0168-9002(03)01368-8`.

[45] J. Allison et al., "Geant4 developments and applications", *IEEE Trans. Nucl. Sci.* **53** (2006) 270, `doi:10.1109/TNS.2006.869826`.

[46] CMS Collaboration, "Particle-flow reconstruction and global event description with the CMS detector", (2017). `arXiv:1706.04965`. Submitted to JINST.

[47] M. Cacciari, G. P. Salam, and G. Soyez, "The anti-k_t jet clustering algorithm", *JHEP* **04** (2008) 063, `doi:10.1088/1126-6708/2008/04/063`, `arXiv:0802.1189`.

[48] M. Cacciari, G. P. Salam, and G. Soyez, "FastJet user manual", *Eur. Phys. J. C* **72** (2012) 1896, `doi:10.1140/epjc/s10052-012-1896-2`, `arXiv:1111.6097`.

[49] M. Cacciari and G. P. Salam, "Pileup subtraction using jet areas", *Phys. Lett. B* **659** (2008) 119, `doi:10.1016/j.physletb.2007.09.077`, `arXiv:0707.1378`.

[50] M. Cacciari, G. P. Salam, and G. Soyez, "The catchment area of jets", *JHEP* **04** (2008) 005, `doi:10.1088/1126-6708/2008/04/005`, `arXiv:0802.1188`.

[51] CMS Collaboration, "Performance of photon reconstruction and identification with the CMS detector in proton-proton collisions at $\sqrt{s} = 8\,\text{TeV}$", *JINST* **10** (2015) P08010, `doi:10.1088/1748-0221/10/08/P08010`, `arXiv:1502.02702`.

[52] R. Fruhwirth, "Application of Kalman filtering to track and vertex fitting", *Nucl. Instrum. Meth. A* **262** (1987) 444, `doi:10.1016/0168-9002(87)90887-4`.

[53] CMS Collaboration, "Determination of jet energy calibration and transverse momentum resolution in CMS", *JINST* **6** (2011) P11002, `doi:10.1088/1748-0221/6/11/P11002`, `arXiv:1107.4277`.

[54] CMS Collaboration, "Jet energy scale and resolution in the CMS experiment in pp collisions at 8 TeV", *JINST* **12** (2017) P02014, `doi:10.1088/1748-0221/12/02/P02014`, `arXiv:1607.03663`.

[55] CMS Collaboration, "Identification of b-quark jets with the CMS experiment", *JINST* **8** (2013) P04013, `doi:10.1088/1748-0221/8/04/P04013`, `arXiv:1211.4462`.

[56] CMS Collaboration, "Identification of b quark jets at the CMS Experiment in the LHC Run 2", CMS Physics Analysis Summary CMS-PAS-BTV-15-001, 2016.

[57] ALEPH, DELPHI, L3, OPAL, SLD Collaborations, LEP Electroweak Working Group, and SLD Electroweak and Heavy Flavour Groups, "Precision electroweak measurements on the Z resonance", *Phys. Rep.* **427** (2006) 257, `doi:10.1016/j.physrep.2005.12.006`.

[58] I. Anderson et al., "Constraining anomalous *HVV* interactions at proton and lepton colliders", *Phys. Rev. D* **89** (2014) 035007, `doi:10.1103/PhysRevD.89.035007`, `arXiv:1309.4819`.

[59] M. Oreglia, "A study of the reactions $\psi' \to \gamma\gamma\psi$". PhD thesis, Stanford University, 1980. SLAC Report SLAC-R-236.

[60] M. Grazzini, S. Kallweit, and D. Rathlev, "ZZ production at the LHC: Fiducial cross sections and distributions in NNLO QCD", *Phys. Lett. B* **750** (2015) 407, `doi:10.1016/j.physletb.2015.09.055`, `arXiv:1507.06257`.

[61] A. Bierweiler, T. Kasprzik, and J. H. Kühn, "Vector-boson pair production at the LHC to $\mathcal{O}(\alpha^3)$ accuracy", *JHEP* **12** (2013) 071, `doi:10.1007/JHEP12(2013)071`, `arXiv:1305.5402`.

[62] M. Bonvini et al., "Signal-background interference effects in $gg \to H \to WW$ beyond leading order", *Phys. Rev. D* **88** (2013) 034032, `doi:10.1103/PhysRevD.88.034032`, `arXiv:1304.3053`.

[63] K. Melnikov and M. Dowling, "Production of two Z-bosons in gluon fusion in the heavy top quark approximation", *Phys. Lett. B* **744** (2015) 43, `doi:10.1016/j.physletb.2015.03.030`, `arXiv:1503.01274`.

[64] C. S. Li, H. T. Li, D. Y. Shao, and J. Wang, "Soft gluon resummation in the signal-background interference process of $gg(\to h^*) \to ZZ$", *JHEP* **08** (2015) 065, `doi:10.1007/JHEP08(2015)065`, `arXiv:1504.02388`.

[65] G. Passarino, "Higgs CAT", *Eur. Phys. J. C* **74** (2014) 2866, `doi:10.1140/epjc/s10052-014-2866-7`, `arXiv:1312.2397`.

[66] S. Catani and M. Grazzini, "Next-to-Next-to-Leading-Order subtraction formalism in hadron collisions and its application to Higgs-boson production at the Large Hadron Collider", *Phys. Rev. Lett.* **98** (2007) 222002, `doi:10.1103/PhysRevLett.98.222002`, `arXiv:hep-ph/0703012`.

[67] M. Grazzini, "NNLO predictions for the Higgs boson signal in the H $\to$ WW $\to \ell\nu\ell\nu$ and H$\to$ ZZ $\to 4\ell$ decay channels", *JHEP* **02** (2008) 043, `doi:10.1088/1126-6708/2008/02/043`, `arXiv:0801.3232`.

[68] L. Landau, "On the energy loss of fast particles by ionization", *J. Phys. (USSR)* **8** (1944) 201.

[69] CMS Collaboration, "CMS luminosity measurements for the 2016 data taking period", CMS Physics Analysis Summary CMS-PAS-LUM-17-001, 2017.

[70] J. Butterworth et al., "PDF4LHC recommendations for LHC Run II", *J. Phys. G* **43** (2016) 023001, `doi:10.1088/0954-3899/43/2/023001`, `arXiv:1510.03865`.

[71] F. Garwood, "Fiducial limits for the poisson distribution", *Biometrika* **28** (1936), no. 3-4, 437, `doi:10.1093/biomet/28.3-4.437`.

[72] ATLAS and CMS Collaborations, LHC Higgs Combination Group, "Procedure for the LHC Higgs boson search combination in Summer 2011", ATL-PHYS-PUB/CMS NOTE 2011-11, 2011/005, CERN, 2011.

[73] G. Cowan, K. Cranmer, E. Gross, and O. Vitells, "Asymptotic formulae for likelihood-based tests of new physics", *Eur. Phys. J. C* **71** (2011) 1554, `doi:10.1140/epjc/s10052-011-1554-0`, `arXiv:1007.1727`.

[74] G. J. Feldman and R. D. Cousins, "Unified approach to the classical statistical analysis of small signals", *Phys. Rev. D* **57** (1998) 3873, `doi:10.1103/PhysRevD.57.3873`, `arXiv:physics/9711021`.

[75] CMS Collaboration, "Measurement of differential cross sections for Higgs boson production in the diphoton decay channel in pp collisions at $\sqrt{s} = 8\,\text{TeV}$", *Eur. Phys. J. C* **76** (2015) 13, `doi:10.1140/epjc/s10052-015-3853-3`.

[76] K. Hamilton, P. Nason, E. Re, and G. Zanderighi, "NNLOPS simulation of Higgs boson production", *JHEP* **10** (2013) 222, `doi:10.1007/JHEP10(2013)222`, `arXiv:1309.0017`.

A The CMS Collaboration

Yerevan Physics Institute, Yerevan, Armenia
A.M. Sirunyan, A. Tumasyan

Institut für Hochenergiephysik, Wien, Austria
W. Adam, F. Ambrogi, E. Asilar, T. Bergauer, J. Brandstetter, E. Brondolin, M. Dragicevic, J. Erö, M. Flechl, M. Friedl, R. Frühwirth[1], V.M. Ghete, J. Grossmann, J. Hrubec, M. Jeitler[1], A. König, N. Krammer, I. Krätschmer, D. Liko, T. Madlener, I. Mikulec, E. Pree, D. Rabady, N. Rad, H. Rohringer, J. Schieck[1], R. Schöfbeck, M. Spanring, D. Spitzbart, W. Waltenberger, J. Wittmann, C.-E. Wulz[1], M. Zarucki

Institute for Nuclear Problems, Minsk, Belarus
V. Chekhovsky, V. Mossolov, J. Suarez Gonzalez

Universiteit Antwerpen, Antwerpen, Belgium
E.A. De Wolf, D. Di Croce, X. Janssen, J. Lauwers, H. Van Haevermaet, P. Van Mechelen, N. Van Remortel

Vrije Universiteit Brussel, Brussel, Belgium
S. Abu Zeid, F. Blekman, J. D'Hondt, I. De Bruyn, J. De Clercq, K. Deroover, G. Flouris, D. Lontkovskyi, S. Lowette, S. Moortgat, L. Moreels, A. Olbrechts, Q. Python, K. Skovpen, S. Tavernier, W. Van Doninck, P. Van Mulders, I. Van Parijs

Université Libre de Bruxelles, Bruxelles, Belgium
H. Brun, B. Clerbaux, G. De Lentdecker, H. Delannoy, G. Fasanella, L. Favart, R. Goldouzian, A. Grebenyuk, G. Karapostoli, T. Lenzi, J. Luetic, T. Maerschalk, A. Marinov, A. Randle-conde, T. Seva, C. Vander Velde, P. Vanlaer, D. Vannerom, R. Yonamine, F. Zenoni, F. Zhang[2]

Ghent University, Ghent, Belgium
A. Cimmino, T. Cornelis, D. Dobur, A. Fagot, M. Gul, I. Khvastunov, D. Poyraz, C. Roskas, S. Salva, M. Tytgat, W. Verbeke, N. Zaganidis

Université Catholique de Louvain, Louvain-la-Neuve, Belgium
H. Bakhshiansohi, O. Bondu, S. Brochet, G. Bruno, A. Caudron, S. De Visscher, C. Delaere, M. Delcourt, B. Francois, A. Giammanco, A. Jafari, M. Komm, G. Krintiras, V. Lemaitre, A. Magitteri, A. Mertens, M. Musich, K. Piotrzkowski, L. Quertenmont, M. Vidal Marono, S. Wertz

Université de Mons, Mons, Belgium
N. Beliy

Centro Brasileiro de Pesquisas Fisicas, Rio de Janeiro, Brazil
W.L. Aldá Júnior, F.L. Alves, G.A. Alves, L. Brito, M. Correa Martins Junior, C. Hensel, A. Moraes, M.E. Pol, P. Rebello Teles

Universidade do Estado do Rio de Janeiro, Rio de Janeiro, Brazil
E. Belchior Batista Das Chagas, W. Carvalho, J. Chinellato[3], A. Custódio, E.M. Da Costa, G.G. Da Silveira[4], D. De Jesus Damiao, S. Fonseca De Souza, L.M. Huertas Guativa, H. Malbouisson, M. Melo De Almeida, C. Mora Herrera, L. Mundim, H. Nogima, A. Santoro, A. Sznajder, E.J. Tonelli Manganote[3], F. Torres Da Silva De Araujo, A. Vilela Pereira

Universidade Estadual Paulista [a], Universidade Federal do ABC [b], São Paulo, Brazil
S. Ahuja[a], C.A. Bernardes[a], T.R. Fernandez Perez Tomei[a], E.M. Gregores[b], P.G. Mercadante[b], S.F. Novaes[a], Sandra S. Padula[a], D. Romero Abad[b], J.C. Ruiz Vargas[a]

Institute for Nuclear Research and Nuclear Energy of Bulgaria Academy of Sciences
A. Aleksandrov, R. Hadjiiska, P. Iaydjiev, M. Misheva, M. Rodozov, M. Shopova, S. Stoykova, G. Sultanov

University of Sofia, Sofia, Bulgaria
A. Dimitrov, I. Glushkov, L. Litov, B. Pavlov, P. Petkov

Beihang University, Beijing, China
W. Fang[5], X. Gao[5]

Institute of High Energy Physics, Beijing, China
M. Ahmad, J.G. Bian, G.M. Chen, H.S. Chen, M. Chen, Y. Chen, C.H. Jiang, D. Leggat, H. Liao, Z. Liu, F. Romeo, S.M. Shaheen, A. Spiezia, J. Tao, C. Wang, Z. Wang, E. Yazgan, H. Zhang, J. Zhao

State Key Laboratory of Nuclear Physics and Technology, Peking University, Beijing, China
Y. Ban, G. Chen, Q. Li, S. Liu, Y. Mao, S.J. Qian, D. Wang, Z. Xu

Universidad de Los Andes, Bogota, Colombia
C. Avila, A. Cabrera, L.F. Chaparro Sierra, C. Florez, C.F. González Hernández, J.D. Ruiz Alvarez

University of Split, Faculty of Electrical Engineering, Mechanical Engineering and Naval Architecture, Split, Croatia
B. Courbon, N. Godinovic, D. Lelas, I. Puljak, P.M. Ribeiro Cipriano, T. Sculac

University of Split, Faculty of Science, Split, Croatia
Z. Antunovic, M. Kovac

Institute Rudjer Boskovic, Zagreb, Croatia
V. Brigljevic, D. Ferencek, K. Kadija, B. Mesic, A. Starodumov[6], T. Susa

University of Cyprus, Nicosia, Cyprus
M.W. Ather, A. Attikis, G. Mavromanolakis, J. Mousa, C. Nicolaou, F. Ptochos, P.A. Razis, H. Rykaczewski

Charles University, Prague, Czech Republic
M. Finger[7], M. Finger Jr.[7]

Universidad San Francisco de Quito, Quito, Ecuador
E. Carrera Jarrin

Academy of Scientific Research and Technology of the Arab Republic of Egypt, Egyptian Network of High Energy Physics, Cairo, Egypt
A.A. Abdelalim[8,9], R. Aly[8], Y. Mohammed[10]

National Institute of Chemical Physics and Biophysics, Tallinn, Estonia
R.K. Dewanjee, M. Kadastik, L. Perrini, M. Raidal, A. Tiko, C. Veelken

Department of Physics, University of Helsinki, Helsinki, Finland
P. Eerola, J. Pekkanen, M. Voutilainen

Helsinki Institute of Physics, Helsinki, Finland
J. Härkönen, T. Järvinen, V. Karimäki, R. Kinnunen, T. Lampén, K. Lassila-Perini, S. Lehti, T. Lindén, P. Luukka, E. Tuominen, J. Tuominiemi, E. Tuovinen

Lappeenranta University of Technology, Lappeenranta, Finland
J. Talvitie, T. Tuuva

IRFU, CEA, Université Paris-Saclay, Gif-sur-Yvette, France
M. Besancon, F. Couderc, M. Dejardin, D. Denegri, J.L. Faure, F. Ferri, S. Ganjour, S. Ghosh, A. Givernaud, P. Gras, G. Hamel de Monchenault, P. Jarry, I. Kucher, E. Locci, M. Machet, J. Malcles, G. Negro, J. Rander, A. Rosowsky, M.Ö. Sahin, M. Titov

Laboratoire Leprince-Ringuet, Ecole polytechnique, CNRS/IN2P3, Université Paris-Saclay, Palaiseau, France
A. Abdulsalam, I. Antropov, S. Baffioni, F. Beaudette, P. Busson, L. Cadamuro, C. Charlot, R. Granier de Cassagnac, M. Jo, S. Lisniak, A. Lobanov, J. Martin Blanco, M. Nguyen, C. Ochando, G. Ortona, P. Paganini, P. Pigard, S. Regnard, R. Salerno, J.B. Sauvan, Y. Sirois, A.G. Stahl Leiton, T. Strebler, Y. Yilmaz, A. Zabi, A. Zghiche

Université de Strasbourg, CNRS, IPHC UMR 7178, F-67000 Strasbourg, France
J.-L. Agram[11], J. Andrea, D. Bloch, J.-M. Brom, M. Buttignol, E.C. Chabert, N. Chanon, C. Collard, E. Conte[11], X. Coubez, J.-C. Fontaine[11], D. Gelé, U. Goerlach, M. Jansová, A.-C. Le Bihan, N. Tonon, P. Van Hove

Centre de Calcul de l'Institut National de Physique Nucleaire et de Physique des Particules, CNRS/IN2P3, Villeurbanne, France
S. Gadrat

Université de Lyon, Université Claude Bernard Lyon 1, CNRS-IN2P3, Institut de Physique Nucléaire de Lyon, Villeurbanne, France
S. Beauceron, C. Bernet, G. Boudoul, R. Chierici, D. Contardo, P. Depasse, H. El Mamouni, J. Fay, L. Finco, S. Gascon, M. Gouzevitch, G. Grenier, B. Ille, F. Lagarde, I.B. Laktineh, M. Lethuillier, L. Mirabito, A.L. Pequegnot, S. Perries, A. Popov[12], V. Sordini, M. Vander Donckt, S. Viret

Georgian Technical University, Tbilisi, Georgia
A. Khvedelidze[7]

Tbilisi State University, Tbilisi, Georgia
Z. Tsamalaidze[7]

RWTH Aachen University, I. Physikalisches Institut, Aachen, Germany
C. Autermann, S. Beranek, L. Feld, M.K. Kiesel, K. Klein, M. Lipinski, M. Preuten, C. Schomakers, J. Schulz, T. Verlage

RWTH Aachen University, III. Physikalisches Institut A, Aachen, Germany
A. Albert, E. Dietz-Laursonn, D. Duchardt, M. Endres, M. Erdmann, S. Erdweg, T. Esch, R. Fischer, A. Güth, M. Hamer, T. Hebbeker, C. Heidemann, K. Hoepfner, S. Knutzen, M. Merschmeyer, A. Meyer, P. Millet, S. Mukherjee, M. Olschewski, K. Padeken, T. Pook, M. Radziej, H. Reithler, M. Rieger, F. Scheuch, D. Teyssier, S. Thüer

RWTH Aachen University, III. Physikalisches Institut B, Aachen, Germany
G. Flügge, B. Kargoll, T. Kress, A. Künsken, J. Lingemann, T. Müller, A. Nehrkorn, A. Nowack, C. Pistone, O. Pooth, A. Stahl[13]

Deutsches Elektronen-Synchrotron, Hamburg, Germany
M. Aldaya Martin, T. Arndt, C. Asawatangtrakuldee, K. Beernaert, O. Behnke, U. Behrens, A. Bermúdez Martínez, A.A. Bin Anuar, K. Borras[14], V. Botta, A. Campbell, P. Connor, C. Contreras-Campana, F. Costanza, C. Diez Pardos, G. Eckerlin, D. Eckstein, T. Eichhorn,

E. Eren, E. Gallo[15], J. Garay Garcia, A. Geiser, A. Gizhko, J.M. Grados Luyando, A. Grohsjean, P. Gunnellini, A. Harb, J. Hauk, M. Hempel[16], H. Jung, A. Kalogeropoulos, M. Kasemann, J. Keaveney, C. Kleinwort, I. Korol, D. Krücker, W. Lange, A. Lelek, T. Lenz, J. Leonard, K. Lipka, W. Lohmann[16], R. Mankel, I.-A. Melzer-Pellmann, A.B. Meyer, G. Mittag, J. Mnich, A. Mussgiller, E. Ntomari, D. Pitzl, A. Raspereza, B. Roland, M. Savitskyi, P. Saxena, R. Shevchenko, S. Spannagel, N. Stefaniuk, G.P. Van Onsem, R. Walsh, Y. Wen, K. Wichmann, C. Wissing, O. Zenaiev

University of Hamburg, Hamburg, Germany
S. Bein, V. Blobel, M. Centis Vignali, T. Dreyer, E. Garutti, D. Gonzalez, J. Haller, A. Hinzmann, M. Hoffmann, A. Karavdina, R. Klanner, R. Kogler, N. Kovalchuk, S. Kurz, T. Lapsien, I. Marchesini, D. Marconi, M. Meyer, M. Niedziela, D. Nowatschin, F. Pantaleo[13], T. Peiffer, A. Perieanu, C. Scharf, P. Schleper, A. Schmidt, S. Schumann, J. Schwandt, J. Sonneveld, H. Stadie, G. Steinbrück, F.M. Stober, M. Stöver, H. Tholen, D. Troendle, E. Usai, L. Vanelderen, A. Vanhoefer, B. Vormwald

Institut für Experimentelle Kernphysik, Karlsruhe, Germany
M. Akbiyik, C. Barth, S. Baur, E. Butz, R. Caspart, T. Chwalek, F. Colombo, W. De Boer, A. Dierlamm, B. Freund, R. Friese, M. Giffels, A. Gilbert, D. Haitz, F. Hartmann[13], S.M. Heindl, U. Husemann, F. Kassel[13], S. Kudella, H. Mildner, M.U. Mozer, Th. Müller, M. Plagge, G. Quast, K. Rabbertz, M. Schröder, I. Shvetsov, G. Sieber, H.J. Simonis, R. Ulrich, S. Wayand, M. Weber, T. Weiler, S. Williamson, C. Wöhrmann, R. Wolf

Institute of Nuclear and Particle Physics (INPP), NCSR Demokritos, Aghia Paraskevi, Greece
G. Anagnostou, G. Daskalakis, T. Geralis, V.A. Giakoumopoulou, A. Kyriakis, D. Loukas, I. Topsis-Giotis

National and Kapodistrian University of Athens, Athens, Greece
G. Karathanasis, S. Kesisoglou, A. Panagiotou, N. Saoulidou

University of Ioánnina, Ioánnina, Greece
I. Evangelou, C. Foudas, P. Kokkas, S. Mallios, N. Manthos, I. Papadopoulos, E. Paradas, J. Strologas, F.A. Triantis

MTA-ELTE Lendület CMS Particle and Nuclear Physics Group, Eötvös Loránd University, Budapest, Hungary
M. Csanad, N. Filipovic, G. Pasztor

Wigner Research Centre for Physics, Budapest, Hungary
G. Bencze, C. Hajdu, D. Horvath[17], Á. Hunyadi, F. Sikler, V. Veszpremi, G. Vesztergombi[18], A.J. Zsigmond

Institute of Nuclear Research ATOMKI, Debrecen, Hungary
N. Beni, S. Czellar, J. Karancsi[19], A. Makovec, J. Molnar, Z. Szillasi

Institute of Physics, University of Debrecen, Debrecen, Hungary
M. Bartók[18], P. Raics, Z.L. Trocsanyi, B. Ujvari

Indian Institute of Science (IISc), Bangalore, India
S. Choudhury, J.R. Komaragiri

National Institute of Science Education and Research, Bhubaneswar, India
S. Bahinipati[20], S. Bhowmik, P. Mal, K. Mandal, A. Nayak[21], D.K. Sahoo[20], N. Sahoo, S.K. Swain

Panjab University, Chandigarh, India
S. Bansal, S.B. Beri, V. Bhatnagar, R. Chawla, N. Dhingra, A.K. Kalsi, A. Kaur, M. Kaur, R. Kumar, P. Kumari, A. Mehta, J.B. Singh, G. Walia

University of Delhi, Delhi, India
Ashok Kumar, Aashaq Shah, A. Bhardwaj, S. Chauhan, B.C. Choudhary, R.B. Garg, S. Keshri, A. Kumar, S. Malhotra, M. Naimuddin, K. Ranjan, R. Sharma, V. Sharma

Saha Institute of Nuclear Physics, HBNI, Kolkata, India
R. Bhardwaj, R. Bhattacharya, S. Bhattacharya, U. Bhawandeep, S. Dey, S. Dutt, S. Dutta, S. Ghosh, N. Majumdar, A. Modak, K. Mondal, S. Mukhopadhyay, S. Nandan, A. Purohit, A. Roy, D. Roy, S. Roy Chowdhury, S. Sarkar, M. Sharan, S. Thakur

Indian Institute of Technology Madras, Madras, India
P.K. Behera

Bhabha Atomic Research Centre, Mumbai, India
R. Chudasama, D. Dutta, V. Jha, V. Kumar, A.K. Mohanty[13], P.K. Netrakanti, L.M. Pant, P. Shukla, A. Topkar

Tata Institute of Fundamental Research-A, Mumbai, India
T. Aziz, S. Dugad, B. Mahakud, S. Mitra, G.B. Mohanty, N. Sur, B. Sutar

Tata Institute of Fundamental Research-B, Mumbai, India
S. Banerjee, S. Bhattacharya, S. Chatterjee, P. Das, M. Guchait, Sa. Jain, S. Kumar, M. Maity[22], G. Majumder, K. Mazumdar, T. Sarkar[22], N. Wickramage[23]

Indian Institute of Science Education and Research (IISER), Pune, India
S. Chauhan, S. Dube, V. Hegde, A. Kapoor, K. Kothekar, S. Pandey, A. Rane, S. Sharma

Institute for Research in Fundamental Sciences (IPM), Tehran, Iran
S. Chenarani[24], E. Eskandari Tadavani, S.M. Etesami[24], M. Khakzad, M. Mohammadi Najafabadi, M. Naseri, S. Paktinat Mehdiabadi[25], F. Rezaei Hosseinabadi, B. Safarzadeh[26], M. Zeinali

University College Dublin, Dublin, Ireland
M. Felcini, M. Grunewald

INFN Sezione di Bari ^{a}, Università di Bari ^{b}, Politecnico di Bari ^{c}, Bari, Italy
M. Abbrescia^{a,b}, C. Calabria^{a,b}, C. Caputo^{a,b}, A. Colaleo^a, D. Creanza^{a,c}, L. Cristella^{a,b}, N. De Filippis^{a,c}, M. De Palma^{a,b}, F. Errico^{a,b}, L. Fiore^a, G. Iaselli^{a,c}, S. Lezki^{a,b}, G. Maggi^{a,c}, M. Maggi^a, G. Miniello^{a,b}, S. My^{a,b}, S. Nuzzo^{a,b}, A. Pompili^{a,b}, G. Pugliese^{a,c}, R. Radogna^{a,b}, A. Ranieri^a, G. Selvaggi^{a,b}, A. Sharma^a, L. Silvestris^{a,13}, R. Venditti^a, P. Verwilligen^a

INFN Sezione di Bologna ^{a}, Università di Bologna ^{b}, Bologna, Italy
G. Abbiendi^a, C. Battilana^{a,b}, D. Bonacorsi^{a,b}, S. Braibant-Giacomelli^{a,b}, R. Campanini^{a,b}, P. Capiluppi^{a,b}, A. Castro^{a,b}, F.R. Cavallo^a, S.S. Chhibra^a, G. Codispoti^{a,b}, M. Cuffiani^{a,b}, G.M. Dallavalle^a, F. Fabbri^a, A. Fanfani^{a,b}, D. Fasanella^{a,b}, P. Giacomelli^a, C. Grandi^a, L. Guiducci^{a,b}, S. Marcellini^a, G. Masetti^a, A. Montanari^a, F.L. Navarria^{a,b}, A. Perrotta^a, A.M. Rossi^{a,b}, T. Rovelli^{a,b}, G.P. Siroli^{a,b}, N. Tosi^a

INFN Sezione di Catania ^{a}, Università di Catania ^{b}, Catania, Italy
S. Albergo^{a,b}, S. Costa^{a,b}, A. Di Mattia^a, F. Giordano^{a,b}, R. Potenza^{a,b}, A. Tricomi^{a,b}, C. Tuve^{a,b}

INFN Sezione di Firenze [a]**, Università di Firenze** [b]**, Firenze, Italy**
G. Barbagli[a], K. Chatterjee[a,b], V. Ciulli[a,b], C. Civinini[a], R. D'Alessandro[a,b], E. Focardi[a,b], P. Lenzi[a,b], M. Meschini[a], S. Paoletti[a], L. Russo[a,27], G. Sguazzoni[a], D. Strom[a], L. Viliani[a,b,13]

INFN Laboratori Nazionali di Frascati, Frascati, Italy
L. Benussi, S. Bianco, F. Fabbri, D. Piccolo, F. Primavera[13]

INFN Sezione di Genova [a]**, Università di Genova** [b]**, Genova, Italy**
V. Calvelli[a,b], F. Ferro[a], E. Robutti[a], S. Tosi[a,b]

INFN Sezione di Milano-Bicocca [a]**, Università di Milano-Bicocca** [b]**, Milano, Italy**
L. Brianza[a,b], F. Brivio[a,b], V. Ciriolo[a,b], M.E. Dinardo[a,b], S. Fiorendi[a,b], S. Gennai[a], A. Ghezzi[a,b], P. Govoni[a,b], M. Malberti[a,b], S. Malvezzi[a], R.A. Manzoni[a,b], D. Menasce[a], L. Moroni[a], M. Paganoni[a,b], K. Pauwels[a,b], D. Pedrini[a], S. Pigazzini[a,b,28], S. Ragazzi[a,b], T. Tabarelli de Fatis[a,b]

INFN Sezione di Napoli [a]**, Università di Napoli 'Federico II'** [b]**, Napoli, Italy, Università della Basilicata** [c]**, Potenza, Italy, Università G. Marconi** [d]**, Roma, Italy**
S. Buontempo[a], N. Cavallo[a,c], S. Di Guida[a,d,13], F. Fabozzi[a,c], F. Fienga[a,b], A.O.M. Iorio[a,b], W.A. Khan[a], L. Lista[a], S. Meola[a,d,13], P. Paolucci[a,13], C. Sciacca[a,b], F. Thyssen[a]

INFN Sezione di Padova [a]**, Università di Padova** [b]**, Padova, Italy, Università di Trento** [c]**, Trento, Italy**
P. Azzi[a,13], L. Benato[a,b], D. Bisello[a,b], A. Boletti[a,b], R. Carlin[a,b], A. Carvalho Antunes De Oliveira[a,b], P. Checchia[a], M. Dall'Osso[a,b], P. De Castro Manzano[a], T. Dorigo[a], U. Dosselli[a], F. Gasparini[a,b], A. Gozzelino[a], S. Lacaprara[a], P. Lujan, M. Margoni[a,b], G. Maron[a,29], A.T. Meneguzzo[a,b], N. Pozzobon[a,b], P. Ronchese[a,b], R. Rossin[a,b], F. Simonetto[a,b], E. Torassa[a], S. Ventura[a], M. Zanetti[a,b], P. Zotto[a,b]

INFN Sezione di Pavia [a]**, Università di Pavia** [b]**, Pavia, Italy**
A. Braghieri[a], F. Fallavollita[a,b], A. Magnani[a,b], P. Montagna[a,b], S.P. Ratti[a,b], V. Re[a], M. Ressegotti, C. Riccardi[a,b], P. Salvini[a], I. Vai[a,b], P. Vitulo[a,b]

INFN Sezione di Perugia [a]**, Università di Perugia** [b]**, Perugia, Italy**
L. Alunni Solestizi[a,b], M. Biasini[a,b], G.M. Bilei[a], C. Cecchi[a,b], D. Ciangottini[a,b], L. Fanò[a,b], P. Lariccia[a,b], R. Leonardi[a,b], E. Manoni[a], G. Mantovani[a,b], V. Mariani[a,b], M. Menichelli[a], A. Rossi[a,b], A. Santocchia[a,b], D. Spiga[a]

INFN Sezione di Pisa [a]**, Università di Pisa** [b]**, Scuola Normale Superiore di Pisa** [c]**, Pisa, Italy**
K. Androsov[a], P. Azzurri[a,13], G. Bagliesi[a], J. Bernardini[a], T. Boccali[a], L. Borrello, R. Castaldi[a], M.A. Ciocci[a,b], R. Dell'Orso[a], G. Fedi[a], L. Giannini[a,c], A. Giassi[a], M.T. Grippo[a,27], F. Ligabue[a,c], T. Lomtadze[a], E. Manca[a,c], G. Mandorli[a,c], L. Martini[a,b], A. Messineo[a,b], F. Palla[a], A. Rizzi[a,b], A. Savoy-Navarro[a,30], P. Spagnolo[a], R. Tenchini[a], G. Tonelli[a,b], A. Venturi[a], P.G. Verdini[a]

INFN Sezione di Roma [a]**, Sapienza Università di Roma** [b]**, Rome, Italy**
L. Barone[a,b], F. Cavallari[a], M. Cipriani[a,b], D. Del Re[a,b,13], M. Diemoz[a], S. Gelli[a,b], E. Longo[a,b], F. Margaroli[a,b], B. Marzocchi[a,b], P. Meridiani[a], G. Organtini[a,b], R. Paramatti[a,b], F. Preiato[a,b], S. Rahatlou[a,b], C. Rovelli[a], F. Santanastasio[a,b]

INFN Sezione di Torino [a]**, Università di Torino** [b]**, Torino, Italy, Università del Piemonte Orientale** [c]**, Novara, Italy**
N. Amapane[a,b], R. Arcidiacono[a,c], S. Argiro[a,b], M. Arneodo[a,c], N. Bartosik[a], R. Bellan[a,b], C. Biino[a], A. Cappati, N. Cartiglia[a], F. Cenna[a,b], M. Costa[a,b], R. Covarelli[a,b], A. Degano[a,b], N. Demaria[a], B. Kiani[a,b], C. Mariotti[a], S. Maselli[a], E. Migliore[a,b], V. Monaco[a,b], E. Monteil[a,b],

M. Monteno[a], M.M. Obertino[a,b], L. Pacher[a,b], N. Pastrone[a], M. Pelliccioni[a], G.L. Pinna Angioni[a,b], F. Ravera[a,b], A. Romero[a,b], M. Ruspa[a,c], R. Sacchi[a,b], K. Shchelina[a,b], V. Sola[a], A. Solano[a,b], A. Staiano[a], P. Traczyk[a,b]

INFN Sezione di Trieste [a], Università di Trieste [b], Trieste, Italy
S. Belforte[a], M. Casarsa[a], F. Cossutti[a], G. Della Ricca[a,b], A. Zanetti[a]

Kyungpook National University, Daegu, Korea
D.H. Kim, G.N. Kim, M.S. Kim, J. Lee, S. Lee, S.W. Lee, C.S. Moon, Y.D. Oh, S. Sekmen, D.C. Son, Y.C. Yang

Chonbuk National University, Jeonju, Korea
A. Lee

Chonnam National University, Institute for Universe and Elementary Particles, Kwangju, Korea
H. Kim, D.H. Moon, G. Oh

Hanyang University, Seoul, Korea
J.A. Brochero Cifuentes, J. Goh, T.J. Kim

Korea University, Seoul, Korea
S. Cho, S. Choi, Y. Go, D. Gyun, S. Ha, B. Hong, Y. Jo, Y. Kim, K. Lee, K.S. Lee, S. Lee, J. Lim, S.K. Park, Y. Roh

Seoul National University, Seoul, Korea
J. Almond, J. Kim, J.S. Kim, H. Lee, K. Lee, K. Nam, S.B. Oh, B.C. Radburn-Smith, S.h. Seo, U.K. Yang, H.D. Yoo, G.B. Yu

University of Seoul, Seoul, Korea
M. Choi, H. Kim, J.H. Kim, J.S.H. Lee, I.C. Park, G. Ryu

Sungkyunkwan University, Suwon, Korea
Y. Choi, C. Hwang, J. Lee, I. Yu

Vilnius University, Vilnius, Lithuania
V. Dudenas, A. Juodagalvis, J. Vaitkus

National Centre for Particle Physics, Universiti Malaya, Kuala Lumpur, Malaysia
I. Ahmed, Z.A. Ibrahim, M.A.B. Md Ali[31], F. Mohamad Idris[32], W.A.T. Wan Abdullah, M.N. Yusli, Z. Zolkapli

Centro de Investigacion y de Estudios Avanzados del IPN, Mexico City, Mexico
Reyes-Almanza, R, Ramirez-Sanchez, G., Duran-Osuna, M. C., H. Castilla-Valdez, E. De La Cruz-Burelo, I. Heredia-De La Cruz[33], Rabadan-Trejo, R. I., R. Lopez-Fernandez, J. Mejia Guisao, A. Sanchez-Hernandez

Universidad Iberoamericana, Mexico City, Mexico
S. Carrillo Moreno, C. Oropeza Barrera, F. Vazquez Valencia

Benemerita Universidad Autonoma de Puebla, Puebla, Mexico
I. Pedraza, H.A. Salazar Ibarguen, C. Uribe Estrada

Universidad Autónoma de San Luis Potosí, San Luis Potosí, Mexico
A. Morelos Pineda

University of Auckland, Auckland, New Zealand
D. Krofcheck

University of Canterbury, Christchurch, New Zealand
P.H. Butler

National Centre for Physics, Quaid-I-Azam University, Islamabad, Pakistan
A. Ahmad, M. Ahmad, Q. Hassan, H.R. Hoorani, A. Saddique, M.A. Shah, M. Shoaib, M. Waqas

National Centre for Nuclear Research, Swierk, Poland
H. Bialkowska, M. Bluj, B. Boimska, T. Frueboes, M. Górski, M. Kazana, K. Nawrocki, K. Romanowska-Rybinska, M. Szleper, P. Zalewski

Institute of Experimental Physics, Faculty of Physics, University of Warsaw, Warsaw, Poland
K. Bunkowski, A. Byszuk[34], K. Doroba, A. Kalinowski, M. Konecki, J. Krolikowski, M. Misiura, M. Olszewski, A. Pyskir, M. Walczak

Laboratório de Instrumentação e Física Experimental de Partículas, Lisboa, Portugal
P. Bargassa, C. Beirão Da Cruz E Silva, B. Calpas[35], A. Di Francesco, P. Faccioli, M. Gallinaro, J. Hollar, N. Leonardo, L. Lloret Iglesias, M.V. Nemallapudi, J. Seixas, O. Toldaiev, D. Vadruccio, J. Varela

Joint Institute for Nuclear Research, Dubna, Russia
S. Afanasiev, P. Bunin, M. Gavrilenko, I. Golutvin, I. Gorbunov, A. Kamenev, V. Karjavin, A. Lanev, A. Malakhov, V. Matveev[36,37], V. Palichik, V. Perelygin, S. Shmatov, S. Shulha, N. Skatchkov, V. Smirnov, N. Voytishin, A. Zarubin

Petersburg Nuclear Physics Institute, Gatchina (St. Petersburg), Russia
Y. Ivanov, V. Kim[38], E. Kuznetsova[39], P. Levchenko, V. Murzin, V. Oreshkin, I. Smirnov, V. Sulimov, L. Uvarov, S. Vavilov, A. Vorobyev

Institute for Nuclear Research, Moscow, Russia
Yu. Andreev, A. Dermenev, S. Gninenko, N. Golubev, A. Karneyeu, M. Kirsanov, N. Krasnikov, A. Pashenkov, D. Tlisov, A. Toropin

Institute for Theoretical and Experimental Physics, Moscow, Russia
V. Epshteyn, V. Gavrilov, N. Lychkovskaya, V. Popov, I. Pozdnyakov, G. Safronov, A. Spiridonov, A. Stepennov, M. Toms, E. Vlasov, A. Zhokin

Moscow Institute of Physics and Technology, Moscow, Russia
T. Aushev, A. Bylinkin[37]

National Research Nuclear University 'Moscow Engineering Physics Institute' (MEPhI), Moscow, Russia
M. Chadeeva[40], O. Markin, P. Parygin, D. Philippov, S. Polikarpov, V. Rusinov, E. Zhemchugov

P.N. Lebedev Physical Institute, Moscow, Russia
V. Andreev, M. Azarkin[37], I. Dremin[37], M. Kirakosyan[37], A. Terkulov

Skobeltsyn Institute of Nuclear Physics, Lomonosov Moscow State University, Moscow, Russia
A. Baskakov, A. Belyaev, E. Boos, V. Bunichev, M. Dubinin[41], L. Dudko, A. Ershov, A. Gribushin, V. Klyukhin, O. Kodolova, I. Lokhtin, I. Miagkov, S. Obraztsov, S. Petrushanko, V. Savrin

Novosibirsk State University (NSU), Novosibirsk, Russia
V. Blinov[42], Y.Skovpen[42], D. Shtol[42]

State Research Center of Russian Federation, Institute for High Energy Physics, Protvino, Russia
I. Azhgirey, I. Bayshev, S. Bitioukov, D. Elumakhov, V. Kachanov, A. Kalinin, D. Konstantinov, V. Krychkine, V. Petrov, R. Ryutin, A. Sobol, S. Troshin, N. Tyurin, A. Uzunian, A. Volkov

University of Belgrade, Faculty of Physics and Vinca Institute of Nuclear Sciences, Belgrade, Serbia
P. Adzic[43], P. Cirkovic, D. Devetak, M. Dordevic, J. Milosevic, V. Rekovic

Centro de Investigaciones Energéticas Medioambientales y Tecnológicas (CIEMAT), Madrid, Spain
J. Alcaraz Maestre, M. Barrio Luna, M. Cerrada, N. Colino, B. De La Cruz, A. Delgado Peris, A. Escalante Del Valle, C. Fernandez Bedoya, J.P. Fernández Ramos, J. Flix, M.C. Fouz, P. Garcia-Abia, O. Gonzalez Lopez, S. Goy Lopez, J.M. Hernandez, M.I. Josa, A. Pérez-Calero Yzquierdo, J. Puerta Pelayo, A. Quintario Olmeda, I. Redondo, L. Romero, M.S. Soares, A. Álvarez Fernández

Universidad Autónoma de Madrid, Madrid, Spain
J.F. de Trocóniz, M. Missiroli, D. Moran

Universidad de Oviedo, Oviedo, Spain
J. Cuevas, C. Erice, J. Fernandez Menendez, I. Gonzalez Caballero, J.R. González Fernández, E. Palencia Cortezon, S. Sanchez Cruz, I. Suárez Andrés, P. Vischia, J.M. Vizan Garcia

Instituto de Física de Cantabria (IFCA), CSIC-Universidad de Cantabria, Santander, Spain
I.J. Cabrillo, A. Calderon, B. Chazin Quero, E. Curras, J. Duarte Campderros, M. Fernandez, J. Garcia-Ferrero, G. Gomez, A. Lopez Virto, J. Marco, C. Martinez Rivero, P. Martinez Ruiz del Arbol, F. Matorras, J. Piedra Gomez, T. Rodrigo, A. Ruiz-Jimeno, L. Scodellaro, N. Trevisani, I. Vila, R. Vilar Cortabitarte

CERN, European Organization for Nuclear Research, Geneva, Switzerland
D. Abbaneo, E. Auffray, P. Baillon, A.H. Ball, D. Barney, M. Bianco, P. Bloch, A. Bocci, C. Botta, T. Camporesi, R. Castello, M. Cepeda, G. Cerminara, E. Chapon, Y. Chen, D. d'Enterria, A. Dabrowski, V. Daponte, A. David, M. De Gruttola, A. De Roeck, E. Di Marco[44], M. Dobson, B. Dorney, T. du Pree, M. Dünser, N. Dupont, A. Elliott-Peisert, P. Everaerts, G. Franzoni, J. Fulcher, W. Funk, D. Gigi, K. Gill, F. Glege, D. Gulhan, S. Gundacker, M. Guthoff, P. Harris, J. Hegeman, V. Innocente, P. Janot, O. Karacheban[16], J. Kieseler, H. Kirschenmann, V. Knünz, A. Kornmayer[13], M.J. Kortelainen, C. Lange, P. Lecoq, C. Lourenço, M.T. Lucchini, L. Malgeri, M. Mannelli, A. Martelli, F. Meijers, J.A. Merlin, S. Mersi, E. Meschi, P. Milenovic[45], F. Moortgat, M. Mulders, H. Neugebauer, S. Orfanelli, L. Orsini, L. Pape, E. Perez, M. Peruzzi, A. Petrilli, G. Petrucciani, A. Pfeiffer, M. Pierini, A. Racz, T. Reis, G. Rolandi[46], M. Rovere, H. Sakulin, C. Schäfer, C. Schwick, M. Seidel, M. Selvaggi, A. Sharma, P. Silva, P. Sphicas[47], A. Stakia, J. Steggemann, M. Stoye, M. Tosi, D. Treille, A. Triossi, A. Tsirou, V. Veckalns[48], G.I. Veres[18], M. Verweij, N. Wardle, W.D. Zeuner

Paul Scherrer Institut, Villigen, Switzerland
W. Bertl†, L. Caminada[49], K. Deiters, W. Erdmann, R. Horisberger, Q. Ingram, H.C. Kaestli, D. Kotlinski, U. Langenegger, T. Rohe, S.A. Wiederkehr

Institute for Particle Physics, ETH Zurich, Zurich, Switzerland
F. Bachmair, L. Bäni, P. Berger, L. Bianchini, B. Casal, G. Dissertori, M. Dittmar, M. Donegà, C. Grab, C. Heidegger, D. Hits, J. Hoss, G. Kasieczka, T. Klijnsma, W. Lustermann, B. Mangano, M. Marionneau, M.T. Meinhard, D. Meister, F. Micheli, P. Musella, F. Nessi-Tedaldi, F. Pandolfi,

J. Pata, F. Pauss, G. Perrin, L. Perrozzi, M. Quittnat, M. Reichmann, M. Schönenberger, L. Shchutska, V.R. Tavolaro, K. Theofilatos, M.L. Vesterbacka Olsson, R. Wallny, D.H. Zhu

Universität Zürich, Zurich, Switzerland
T.K. Aarrestad, C. Amsler[50], M.F. Canelli, A. De Cosa, R. Del Burgo, S. Donato, C. Galloni, T. Hreus, B. Kilminster, J. Ngadiuba, D. Pinna, G. Rauco, P. Robmann, D. Salerno, C. Seitz, Y. Takahashi, A. Zucchetta

National Central University, Chung-Li, Taiwan
V. Candelise, T.H. Doan, Sh. Jain, R. Khurana, C.M. Kuo, W. Lin, A. Pozdnyakov, S.S. Yu

National Taiwan University (NTU), Taipei, Taiwan
Arun Kumar, P. Chang, Y. Chao, K.F. Chen, P.H. Chen, F. Fiori, W.-S. Hou, Y. Hsiung, Y.F. Liu, R.-S. Lu, E. Paganis, A. Psallidas, A. Steen, J.f. Tsai

Chulalongkorn University, Faculty of Science, Department of Physics, Bangkok, Thailand
B. Asavapibhop, K. Kovitanggoon, G. Singh, N. Srimanobhas

ukurova University, Physics Department, Science and Art Faculty, Adana, Turkey
A. Adiguzel[51], F. Boran, S. Cerci[52], S. Damarseckin, Z.S. Demiroglu, C. Dozen, I. Dumanoglu, S. Girgis, G. Gokbulut, Y. Guler, I. Hos[53], E.E. Kangal[54], O. Kara, A. Kayis Topaksu, U. Kiminsu, M. Oglakci, G. Onengut[55], K. Ozdemir[56], D. Sunar Cerci[52], B. Tali[52], S. Turkcapar, I.S. Zorbakir, C. Zorbilmez

Middle East Technical University, Physics Department, Ankara, Turkey
B. Bilin, G. Karapinar[57], K. Ocalan[58], M. Yalvac, M. Zeyrek

Bogazici University, Istanbul, Turkey
E. Gülmez, M. Kaya[59], O. Kaya[60], S. Tekten, E.A. Yetkin[61]

Istanbul Technical University, Istanbul, Turkey
M.N. Agaras, S. Atay, A. Cakir, K. Cankocak

Institute for Scintillation Materials of National Academy of Science of Ukraine, Kharkov, Ukraine
B. Grynyov

National Scientific Center, Kharkov Institute of Physics and Technology, Kharkov, Ukraine
L. Levchuk, P. Sorokin

University of Bristol, Bristol, United Kingdom
R. Aggleton, F. Ball, L. Beck, J.J. Brooke, D. Burns, E. Clement, D. Cussans, O. Davignon, H. Flacher, J. Goldstein, M. Grimes, G.P. Heath, H.F. Heath, J. Jacob, L. Kreczko, C. Lucas, D.M. Newbold[62], S. Paramesvaran, A. Poll, T. Sakuma, S. Seif El Nasr-storey, D. Smith, V.J. Smith

Rutherford Appleton Laboratory, Didcot, United Kingdom
K.W. Bell, A. Belyaev[63], C. Brew, R.M. Brown, L. Calligaris, D. Cieri, D.J.A. Cockerill, J.A. Coughlan, K. Harder, S. Harper, E. Olaiya, D. Petyt, C.H. Shepherd-Themistocleous, A. Thea, I.R. Tomalin, T. Williams

Imperial College, London, United Kingdom
G. Auzinger, R. Bainbridge, S. Breeze, O. Buchmuller, A. Bundock, S. Casasso, M. Citron, D. Colling, L. Corpe, P. Dauncey, G. Davies, A. De Wit, M. Della Negra, R. Di Maria, A. Elwood, Y. Haddad, G. Hall, G. Iles, T. James, R. Lane, C. Laner, L. Lyons, A.-M. Magnan, S. Malik, L. Mastrolorenzo, T. Matsushita, J. Nash, A. Nikitenko[6], V. Palladino, M. Pesaresi,

D.M. Raymond, A. Richards, A. Rose, E. Scott, C. Seez, A. Shtipliyski, S. Summers, A. Tapper, K. Uchida, M. Vazquez Acosta[64], T. Virdee[13], D. Winterbottom, J. Wright, S.C. Zenz

Brunel University, Uxbridge, United Kingdom
J.E. Cole, P.R. Hobson, A. Khan, P. Kyberd, I.D. Reid, P. Symonds, L. Teodorescu, M. Turner

Baylor University, Waco, USA
A. Borzou, K. Call, J. Dittmann, K. Hatakeyama, H. Liu, N. Pastika, C. Smith

Catholic University of America, Washington DC, USA
R. Bartek, A. Dominguez

The University of Alabama, Tuscaloosa, USA
A. Buccilli, S.I. Cooper, C. Henderson, P. Rumerio, C. West

Boston University, Boston, USA
D. Arcaro, A. Avetisyan, T. Bose, D. Gastler, D. Rankin, C. Richardson, J. Rohlf, L. Sulak, D. Zou

Brown University, Providence, USA
G. Benelli, D. Cutts, A. Garabedian, J. Hakala, U. Heintz, J.M. Hogan, K.H.M. Kwok, E. Laird, G. Landsberg, Z. Mao, M. Narain, S. Piperov, S. Sagir, R. Syarif, D. Yu

University of California, Davis, Davis, USA
R. Band, C. Brainerd, D. Burns, M. Calderon De La Barca Sanchez, M. Chertok, J. Conway, R. Conway, P.T. Cox, R. Erbacher, C. Flores, G. Funk, M. Gardner, W. Ko, R. Lander, C. Mclean, M. Mulhearn, D. Pellett, J. Pilot, S. Shalhout, M. Shi, J. Smith, M. Squires, D. Stolp, K. Tos, M. Tripathi, Z. Wang

University of California, Los Angeles, USA
M. Bachtis, C. Bravo, R. Cousins, A. Dasgupta, A. Florent, J. Hauser, M. Ignatenko, N. Mccoll, D. Saltzberg, C. Schnaible, V. Valuev

University of California, Riverside, Riverside, USA
E. Bouvier, K. Burt, R. Clare, J. Ellison, J.W. Gary, S.M.A. Ghiasi Shirazi, G. Hanson, J. Heilman, P. Jandir, E. Kennedy, F. Lacroix, O.R. Long, M. Olmedo Negrete, M.I. Paneva, A. Shrinivas, W. Si, L. Wang, H. Wei, S. Wimpenny, B. R. Yates

University of California, San Diego, La Jolla, USA
J.G. Branson, S. Cittolin, M. Derdzinski, B. Hashemi, A. Holzner, D. Klein, G. Kole, V. Krutelyov, J. Letts, I. Macneill, M. Masciovecchio, D. Olivito, S. Padhi, M. Pieri, M. Sani, V. Sharma, S. Simon, M. Tadel, A. Vartak, S. Wasserbaech[65], J. Wood, F. Würthwein, A. Yagil, G. Zevi Della Porta

University of California, Santa Barbara - Department of Physics, Santa Barbara, USA
N. Amin, R. Bhandari, J. Bradmiller-Feld, C. Campagnari, A. Dishaw, V. Dutta, M. Franco Sevilla, C. George, F. Golf, L. Gouskos, J. Gran, R. Heller, J. Incandela, S.D. Mullin, A. Ovcharova, H. Qu, J. Richman, D. Stuart, I. Suarez, J. Yoo

California Institute of Technology, Pasadena, USA
D. Anderson, J. Bendavid, A. Bornheim, J.M. Lawhorn, H.B. Newman, T. Nguyen, C. Pena, M. Spiropulu, J.R. Vlimant, S. Xie, Z. Zhang, R.Y. Zhu

Carnegie Mellon University, Pittsburgh, USA
M.B. Andrews, T. Ferguson, T. Mudholkar, M. Paulini, J. Russ, M. Sun, H. Vogel, I. Vorobiev, M. Weinberg

University of Colorado Boulder, Boulder, USA
J.P. Cumalat, W.T. Ford, F. Jensen, A. Johnson, M. Krohn, S. Leontsinis, T. Mulholland, K. Stenson, S.R. Wagner

Cornell University, Ithaca, USA
J. Alexander, J. Chaves, J. Chu, S. Dittmer, K. Mcdermott, N. Mirman, J.R. Patterson, A. Rinkevicius, A. Ryd, L. Skinnari, L. Soffi, S.M. Tan, Z. Tao, J. Thom, J. Tucker, P. Wittich, M. Zientek

Fermi National Accelerator Laboratory, Batavia, USA
S. Abdullin, M. Albrow, G. Apollinari, A. Apresyan, A. Apyan, S. Banerjee, L.A.T. Bauerdick, A. Beretvas, J. Berryhill, P.C. Bhat, G. Bolla, K. Burkett, J.N. Butler, A. Canepa, G.B. Cerati, H.W.K. Cheung, F. Chlebana, M. Cremonesi, J. Duarte, V.D. Elvira, J. Freeman, Z. Gecse, E. Gottschalk, L. Gray, D. Green, S. Grünendahl, O. Gutsche, R.M. Harris, S. Hasegawa, J. Hirschauer, Z. Hu, B. Jayatilaka, S. Jindariani, M. Johnson, U. Joshi, B. Klima, B. Kreis, S. Lammel, D. Lincoln, R. Lipton, M. Liu, T. Liu, R. Lopes De Sá, J. Lykken, K. Maeshima, N. Magini, J.M. Marraffino, S. Maruyama, D. Mason, P. McBride, P. Merkel, S. Mrenna, S. Nahn, V. O'Dell, K. Pedro, O. Prokofyev, G. Rakness, L. Ristori, B. Schneider, E. Sexton-Kennedy, A. Soha, W.J. Spalding, L. Spiegel, S. Stoynev, J. Strait, N. Strobbe, L. Taylor, S. Tkaczyk, N.V. Tran, L. Uplegger, E.W. Vaandering, C. Vernieri, M. Verzocchi, R. Vidal, M. Wang, H.A. Weber, A. Whitbeck

University of Florida, Gainesville, USA
D. Acosta, P. Avery, P. Bortignon, D. Bourilkov, A. Brinkerhoff, A. Carnes, M. Carver, D. Curry, R.D. Field, I.K. Furic, J. Konigsberg, A. Korytov, K. Kotov, P. Ma, K. Matchev, H. Mei, G. Mitselmakher, D. Rank, D. Sperka, N. Terentyev, L. Thomas, J. Wang, S. Wang, J. Yelton

Florida International University, Miami, USA
Y.R. Joshi, S. Linn, P. Markowitz, J.L. Rodriguez

Florida State University, Tallahassee, USA
A. Ackert, T. Adams, A. Askew, S. Hagopian, V. Hagopian, K.F. Johnson, T. Kolberg, G. Martinez, T. Perry, H. Prosper, A. Saha, A. Santra, R. Yohay

Florida Institute of Technology, Melbourne, USA
M.M. Baarmand, V. Bhopatkar, S. Colafranceschi, M. Hohlmann, D. Noonan, T. Roy, F. Yumiceva

University of Illinois at Chicago (UIC), Chicago, USA
M.R. Adams, L. Apanasevich, D. Berry, R.R. Betts, R. Cavanaugh, X. Chen, O. Evdokimov, C.E. Gerber, D.A. Hangal, D.J. Hofman, K. Jung, J. Kamin, I.D. Sandoval Gonzalez, M.B. Tonjes, H. Trauger, N. Varelas, H. Wang, Z. Wu, J. Zhang

The University of Iowa, Iowa City, USA
B. Bilki[66], W. Clarida, K. Dilsiz[67], S. Durgut, R.P. Gandrajula, M. Haytmyradov, V. Khristenko, J.-P. Merlo, H. Mermerkaya[68], A. Mestvirishvili, A. Moeller, J. Nachtman, H. Ogul[69], Y. Onel, F. Ozok[70], A. Penzo, C. Snyder, E. Tiras, J. Wetzel, K. Yi

Johns Hopkins University, Baltimore, USA
B. Blumenfeld, A. Cocoros, N. Eminizer, D. Fehling, L. Feng, A.V. Gritsan, P. Maksimovic, J. Roskes, U. Sarica, M. Swartz, M. Xiao, C. You

The University of Kansas, Lawrence, USA
A. Al-bataineh, P. Baringer, A. Bean, S. Boren, J. Bowen, J. Castle, S. Khalil, A. Kropivnitskaya,

D. Majumder, W. Mcbrayer, M. Murray, C. Royon, S. Sanders, E. Schmitz, R. Stringer, J.D. Tapia Takaki, Q. Wang

Kansas State University, Manhattan, USA
A. Ivanov, K. Kaadze, Y. Maravin, A. Mohammadi, L.K. Saini, N. Skhirtladze, S. Toda

Lawrence Livermore National Laboratory, Livermore, USA
F. Rebassoo, D. Wright

University of Maryland, College Park, USA
C. Anelli, A. Baden, O. Baron, A. Belloni, B. Calvert, S.C. Eno, C. Ferraioli, N.J. Hadley, S. Jabeen, G.Y. Jeng, R.G. Kellogg, J. Kunkle, A.C. Mignerey, F. Ricci-Tam, Y.H. Shin, A. Skuja, S.C. Tonwar

Massachusetts Institute of Technology, Cambridge, USA
D. Abercrombie, B. Allen, V. Azzolini, R. Barbieri, A. Baty, R. Bi, S. Brandt, W. Busza, I.A. Cali, M. D'Alfonso, Z. Demiragli, G. Gomez Ceballos, M. Goncharov, D. Hsu, Y. Iiyama, G.M. Innocenti, M. Klute, D. Kovalskyi, Y.S. Lai, Y.-J. Lee, A. Levin, P.D. Luckey, B. Maier, A.C. Marini, C. Mcginn, C. Mironov, S. Narayanan, X. Niu, C. Paus, C. Roland, G. Roland, J. Salfeld-Nebgen, G.S.F. Stephans, K. Tatar, D. Velicanu, J. Wang, T.W. Wang, B. Wyslouch

University of Minnesota, Minneapolis, USA
A.C. Benvenuti, R.M. Chatterjee, A. Evans, P. Hansen, S. Kalafut, Y. Kubota, Z. Lesko, J. Mans, S. Nourbakhsh, N. Ruckstuhl, R. Rusack, J. Turkewitz

University of Mississippi, Oxford, USA
J.G. Acosta, S. Oliveros

University of Nebraska-Lincoln, Lincoln, USA
E. Avdeeva, K. Bloom, D.R. Claes, C. Fangmeier, R. Gonzalez Suarez, R. Kamalieddin, I. Kravchenko, J. Monroy, J.E. Siado, G.R. Snow, B. Stieger

State University of New York at Buffalo, Buffalo, USA
M. Alyari, J. Dolen, A. Godshalk, C. Harrington, I. Iashvili, D. Nguyen, A. Parker, S. Rappoccio, B. Roozbahani

Northeastern University, Boston, USA
G. Alverson, E. Barberis, A. Hortiangtham, A. Massironi, D.M. Morse, D. Nash, T. Orimoto, R. Teixeira De Lima, D. Trocino, D. Wood

Northwestern University, Evanston, USA
S. Bhattacharya, O. Charaf, K.A. Hahn, N. Mucia, N. Odell, B. Pollack, M.H. Schmitt, K. Sung, M. Trovato, M. Velasco

University of Notre Dame, Notre Dame, USA
N. Dev, M. Hildreth, K. Hurtado Anampa, C. Jessop, D.J. Karmgard, N. Kellams, K. Lannon, N. Loukas, N. Marinelli, F. Meng, C. Mueller, Y. Musienko[36], M. Planer, A. Reinsvold, R. Ruchti, G. Smith, S. Taroni, M. Wayne, M. Wolf, A. Woodard

The Ohio State University, Columbus, USA
J. Alimena, L. Antonelli, B. Bylsma, L.S. Durkin, S. Flowers, B. Francis, A. Hart, C. Hill, W. Ji, B. Liu, W. Luo, D. Puigh, B.L. Winer, H.W. Wulsin

Princeton University, Princeton, USA
A. Benaglia, S. Cooperstein, O. Driga, P. Elmer, J. Hardenbrook, P. Hebda, S. Higginbotham,

D. Lange, J. Luo, D. Marlow, K. Mei, I. Ojalvo, J. Olsen, C. Palmer, P. Piroué, D. Stickland, C. Tully

University of Puerto Rico, Mayaguez, USA
S. Malik, S. Norberg

Purdue University, West Lafayette, USA
A. Barker, V.E. Barnes, S. Das, S. Folgueras, L. Gutay, M.K. Jha, M. Jones, A.W. Jung, A. Khatiwada, D.H. Miller, N. Neumeister, C.C. Peng, J.F. Schulte, J. Sun, F. Wang, W. Xie

Purdue University Northwest, Hammond, USA
T. Cheng, N. Parashar, J. Stupak

Rice University, Houston, USA
A. Adair, B. Akgun, Z. Chen, K.M. Ecklund, F.J.M. Geurts, M. Guilbaud, W. Li, B. Michlin, M. Northup, B.P. Padley, J. Roberts, J. Rorie, Z. Tu, J. Zabel

University of Rochester, Rochester, USA
A. Bodek, P. de Barbaro, R. Demina, Y.t. Duh, T. Ferbel, M. Galanti, A. Garcia-Bellido, J. Han, O. Hindrichs, A. Khukhunaishvili, K.H. Lo, P. Tan, M. Verzetti

The Rockefeller University, New York, USA
R. Ciesielski, K. Goulianos, C. Mesropian

Rutgers, The State University of New Jersey, Piscataway, USA
A. Agapitos, J.P. Chou, Y. Gershtein, T.A. Gómez Espinosa, E. Halkiadakis, M. Heindl, E. Hughes, S. Kaplan, R. Kunnawalkam Elayavalli, S. Kyriacou, A. Lath, R. Montalvo, K. Nash, M. Osherson, H. Saka, S. Salur, S. Schnetzer, D. Sheffield, S. Somalwar, R. Stone, S. Thomas, P. Thomassen, M. Walker

University of Tennessee, Knoxville, USA
A.G. Delannoy, M. Foerster, J. Heideman, G. Riley, K. Rose, S. Spanier, K. Thapa

Texas A&M University, College Station, USA
O. Bouhali[71], A. Castaneda Hernandez[71], A. Celik, M. Dalchenko, M. De Mattia, A. Delgado, S. Dildick, R. Eusebi, J. Gilmore, T. Huang, T. Kamon[72], R. Mueller, Y. Pakhotin, R. Patel, A. Perloff, L. Perniè, D. Rathjens, A. Safonov, A. Tatarinov, K.A. Ulmer

Texas Tech University, Lubbock, USA
N. Akchurin, J. Damgov, F. De Guio, P.R. Dudero, J. Faulkner, E. Gurpinar, S. Kunori, K. Lamichhane, S.W. Lee, T. Libeiro, T. Peltola, S. Undleeb, I. Volobouev, Z. Wang

Vanderbilt University, Nashville, USA
S. Greene, A. Gurrola, R. Janjam, W. Johns, C. Maguire, A. Melo, H. Ni, P. Sheldon, S. Tuo, J. Velkovska, Q. Xu

University of Virginia, Charlottesville, USA
M.W. Arenton, P. Barria, B. Cox, R. Hirosky, A. Ledovskoy, H. Li, C. Neu, T. Sinthuprasith, X. Sun, Y. Wang, E. Wolfe, F. Xia

Wayne State University, Detroit, USA
R. Harr, P.E. Karchin, J. Sturdy, S. Zaleski

University of Wisconsin - Madison, Madison, WI, USA
M. Brodski, J. Buchanan, C. Caillol, S. Dasu, L. Dodd, S. Duric, B. Gomber, M. Grothe,

M. Herndon, A. Hervé, U. Hussain, P. Klabbers, A. Lanaro, A. Levine, K. Long, R. Loveless, G.A. Pierro, G. Polese, T. Ruggles, A. Savin, N. Smith, W.H. Smith, D. Taylor, N. Woods

†: Deceased
1: Also at Vienna University of Technology, Vienna, Austria
2: Also at State Key Laboratory of Nuclear Physics and Technology, Peking University, Beijing, China
3: Also at Universidade Estadual de Campinas, Campinas, Brazil
4: Also at Universidade Federal de Pelotas, Pelotas, Brazil
5: Also at Université Libre de Bruxelles, Bruxelles, Belgium
6: Also at Institute for Theoretical and Experimental Physics, Moscow, Russia
7: Also at Joint Institute for Nuclear Research, Dubna, Russia
8: Also at Helwan University, Cairo, Egypt
9: Now at Zewail City of Science and Technology, Zewail, Egypt
10: Now at Fayoum University, El-Fayoum, Egypt
11: Also at Université de Haute Alsace, Mulhouse, France
12: Also at Skobeltsyn Institute of Nuclear Physics, Lomonosov Moscow State University, Moscow, Russia
13: Also at CERN, European Organization for Nuclear Research, Geneva, Switzerland
14: Also at RWTH Aachen University, III. Physikalisches Institut A, Aachen, Germany
15: Also at University of Hamburg, Hamburg, Germany
16: Also at Brandenburg University of Technology, Cottbus, Germany
17: Also at Institute of Nuclear Research ATOMKI, Debrecen, Hungary
18: Also at MTA-ELTE Lendület CMS Particle and Nuclear Physics Group, Eötvös Loránd University, Budapest, Hungary
19: Also at Institute of Physics, University of Debrecen, Debrecen, Hungary
20: Also at Indian Institute of Technology Bhubaneswar, Bhubaneswar, India
21: Also at Institute of Physics, Bhubaneswar, India
22: Also at University of Visva-Bharati, Santiniketan, India
23: Also at University of Ruhuna, Matara, Sri Lanka
24: Also at Isfahan University of Technology, Isfahan, Iran
25: Also at Yazd University, Yazd, Iran
26: Also at Plasma Physics Research Center, Science and Research Branch, Islamic Azad University, Tehran, Iran
27: Also at Università degli Studi di Siena, Siena, Italy
28: Also at INFN Sezione di Milano-Bicocca; Università di Milano-Bicocca, Milano, Italy
29: Also at Laboratori Nazionali di Legnaro dell'INFN, Legnaro, Italy
30: Also at Purdue University, West Lafayette, USA
31: Also at International Islamic University of Malaysia, Kuala Lumpur, Malaysia
32: Also at Malaysian Nuclear Agency, MOSTI, Kajang, Malaysia
33: Also at Consejo Nacional de Ciencia y Tecnología, Mexico city, Mexico
34: Also at Warsaw University of Technology, Institute of Electronic Systems, Warsaw, Poland
35: Also at Czech Technical University, Praha, Czech Republic
36: Also at Institute for Nuclear Research, Moscow, Russia
37: Now at National Research Nuclear University 'Moscow Engineering Physics Institute' (MEPhI), Moscow, Russia
38: Also at St. Petersburg State Polytechnical University, St. Petersburg, Russia
39: Also at University of Florida, Gainesville, USA
40: Also at P.N. Lebedev Physical Institute, Moscow, Russia
41: Also at California Institute of Technology, Pasadena, USA

42: Also at Budker Institute of Nuclear Physics, Novosibirsk, Russia
43: Also at Faculty of Physics, University of Belgrade, Belgrade, Serbia
44: Also at INFN Sezione di Roma; Sapienza Università di Roma, Rome, Italy
45: Also at University of Belgrade, Faculty of Physics and Vinca Institute of Nuclear Sciences, Belgrade, Serbia
46: Also at Scuola Normale e Sezione dell'INFN, Pisa, Italy
47: Also at National and Kapodistrian University of Athens, Athens, Greece
48: Also at Riga Technical University, Riga, Latvia
49: Also at Universität Zürich, Zurich, Switzerland
50: Also at Stefan Meyer Institute for Subatomic Physics (SMI), Vienna, Austria
51: Also at Istanbul University, Faculty of Science, Istanbul, Turkey
52: Also at Adiyaman University, Adiyaman, Turkey
53: Also at Istanbul Aydin University, Istanbul, Turkey
54: Also at Mersin University, Mersin, Turkey
55: Also at Cag University, Mersin, Turkey
56: Also at Piri Reis University, Istanbul, Turkey
57: Also at Izmir Institute of Technology, Izmir, Turkey
58: Also at Necmettin Erbakan University, Konya, Turkey
59: Also at Marmara University, Istanbul, Turkey
60: Also at Kafkas University, Kars, Turkey
61: Also at Istanbul Bilgi University, Istanbul, Turkey
62: Also at Rutherford Appleton Laboratory, Didcot, United Kingdom
63: Also at School of Physics and Astronomy, University of Southampton, Southampton, United Kingdom
64: Also at Instituto de Astrofísica de Canarias, La Laguna, Spain
65: Also at Utah Valley University, Orem, USA
66: Also at Beykent University, Istanbul, Turkey
67: Also at Bingol University, Bingol, Turkey
68: Also at Erzincan University, Erzincan, Turkey
69: Also at Sinop University, Sinop, Turkey
70: Also at Mimar Sinan University, Istanbul, Istanbul, Turkey
71: Also at Texas A&M University at Qatar, Doha, Qatar
72: Also at Kyungpook National University, Daegu, Korea